


POKER FLAT INCOHERENT SCATTER RADAR INVESTIGATIONS OF THE
NIGHTTIME E-REGION

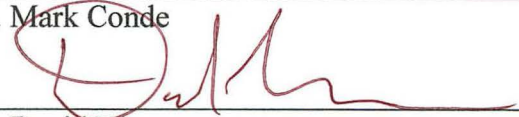
By

Robin L. Whittier

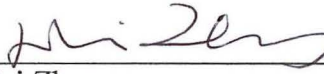
RECOMMENDED:



Dr. Mark Conde




Dr. David Newman



Dr. Hui Zhang

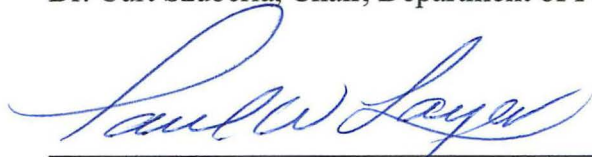


Dr. Roman Makarevich, Advisory Committee Chair

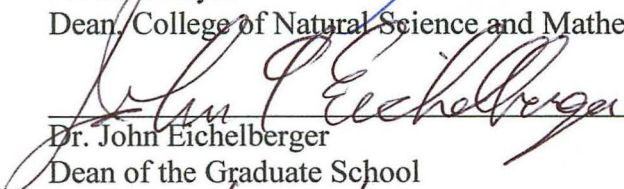


Dr. Curt Szuberla, Chair, Department of Physics


APPROVED:



Dr. Paul Layer
Dean, College of Natural Science and Mathematics



Dr. John Eichelberger
Dean of the Graduate School



Date

POKER FLAT INCOHERENT SCATTER RADAR INVESTIGATIONS OF THE
NIGHTTIME E-REGION

A
THESIS

Presented to the Faculty
of the University of Alaska Fairbanks

in Partial Fulfillment of the Requirements
for the Degree of

MASTER OF SCIENCE

By

Robin L. Whittier, B.A.

Fairbanks, Alaska

May 2014

Abstract

Plasma within the ionosphere affects technology, such as long distance communications and satellite navigation, by scattering and altering the propagation of radio waves sent through the ionosphere. Understanding the structure and dynamics of the ionosphere that may interfere with modern technology is therefore an important aspect of Space Weather research. In this thesis, the average characteristics and dynamics of the nighttime E-region (90–150 km in altitude) are investigated during auroral disturbances and near extreme solar minimum. The near-continuous data on electron density obtained with the Poker Flat Incoherent Scatter Radar (PFISR) near Fairbanks, Alaska are utilized. A number of correlation analyses between E-region electron content and AE index are performed in order to examine the influence of geomagnetic conditions on the E-region in relation to time of the day as well as seasonal and solar cycle effects. It is shown that E-region electron content and AE index exhibit significant positive correlation, particularly near local magnetic midnight, with greater correlation generally occurring in spring and autumn. The midnight feature is interpreted as an indication that the electrojet system near midnight is mostly controlled by electric conductance. The presented statistical results on the current-conductance relationship utilizing a new dataset strengthen conclusions derived from previous studies. The extent of E-region contribution to the total electron content (TEC) is also estimated and investigated for various conditions for the first time using the full altitude profile of PFISR. The estimates ranged between 5%–60% and more active periods generally displayed a more significant contribution from the E-region to TEC. Additionally, using the AE index as an indicator of auroral disturbance onset, the evolution of auroral density enhancements is explored using the superposed epoch analysis technique. The behavior of E-region electron content, peak density, height of peak density, and layer thickness is considered and three discernible phases in response of the thick E-layer to auroral disturbances are found. The observations are consistent with a scenario in which an initially soft and broad auroral electron energy spectrum quickly hardens and narrows during the main response and then slowly softens and becomes more broad during recovery.

Table of Contents

| | Page |
|---|------|
| Signature Page | i |
| Title Page | iii |
| Abstract | v |
| Table of Contents | vii |
| List of Figures | ix |
| List of Tables | xi |
| List of Abbreviations | xiii |
| Acknowledgements..... | xv |
| | |
| 1. Introduction..... | 1 |
| 1.1 Solar-Terrestrial Environment..... | 1 |
| 1.2 The Earth’s Ionosphere | 3 |
| 1.2.1 Ionospheric Regions..... | 3 |
| 1.2.2 Ionospheric Electron Density: A Brief Survey of Past Observations | 5 |
| 1.2.3 Ionospheric Current Systems | 10 |
| 1.3 Observational Techniques and Models | 12 |
| 1.3.1 Coherent Radar Observations of Plasma Irregularities..... | 12 |
| 1.3.2 Incoherent Radar Measurements of Plasma Parameters | 13 |
| 1.3.3 GPS TEC Measurements | 14 |
| 1.3.4 TIMED-SABER Measurements of E-region Density..... | 15 |
| 1.3.5 IRI and STORM-E Models..... | 16 |
| 1.4 Motivation, Aims, and Objectives..... | 17 |
| 2. Instrumentation | 19 |
| 2.1 Incoherent Scatter Radar | 19 |
| 2.1.1 Incoherent Scatter Principles | 19 |
| 2.1.2 Data Processing/Spectrum Analysis | 21 |
| 2.1.3 Poker Flat Incoherent Scatter Radar | 23 |
| 2.2 Magnetometry | 26 |
| 2.2.1 Fluxgate Magnetometer | 26 |
| 2.2.2 Derivation of AE Index..... | 28 |

| | Page |
|--|------|
| 3. Dynamics of Nighttime E-Region Electron Content | 33 |
| 3.1 Determination of Electron Content and Corresponding AE Index | 33 |
| 3.2 ITEC-AE Relationship: Diurnal and Seasonal Variations | 39 |
| 3.3 ITEC-AE Relationship: Solar Zenith Angle Effects | 43 |
| 3.4 E-region Contribution to the Total Electron Content | 45 |
| 3.5 Discussion and Summary | 49 |
| 4. Superposed Epoch Analysis of Nighttime E-Region Disturbances | 53 |
| 4.1 Disturbance Event Selection and Epoch Alignment | 53 |
| 4.2 Quiet-Time Background Contribution | 59 |
| 4.3 SEA with Quiet-Time Contribution Removed | 62 |
| 4.4 Discussion and Summary | 68 |
| 5. Conclusions | 73 |
| References | 75 |

List of Figures

| | Page |
|---|------|
| Figure 1.1: The three regions of the ionosphere. | 4 |
| Figure 1.2: Electron density profiles under various conditions | 6 |
| Figure 1.3: Diurnal variation of the electron density | 7 |
| Figure 1.4: Major ionospheric current systems..... | 11 |
| Figure 2.1: Example of incoherent scatter signal spectrum. | 21 |
| Figure 2.2: PFISR and local instrumentation around Poker Flat. | 24 |
| Figure 2.3: Auroral electrojet index measurements for May 15, 2007 | 29 |
| Figure 3.1: Electron density, electron content, and AE variations on May 1, 2007 | 34 |
| Figure 3.2: Nighttime electron content and AE index in May 2007 | 36 |
| Figure 3.3: Nighttime electron content and AE index in year 2007 | 37 |
| Figure 3.4: Average E-region electron content and AE index..... | 38 |
| Figure 3.5: E-region electron content versus AE index for May 2007 | 40 |
| Figure 3.6: E-region electron content versus AE index for each hour..... | 41 |
| Figure 3.7: Correlation between E-region electron content and AE index versus UT | 42 |
| Figure 3.8: E-region electron content versus AE index for May 2007 | 43 |
| Figure 3.9: E-region electron content versus AE index sorted in SZA | 44 |
| Figure 3.10: Correlation between E-region electron content and AE index versus SZA. | 45 |
| Figure 3.11: E-region contribution to TEC in May 2007. | 47 |
| Figure 3.12: E-region contribution to TEC in 2007–2010..... | 48 |
| Figure 4.1: Distribution of selected events. | 54 |
| Figure 4.2: Superposed epoch analysis. | 55 |
| Figure 4.3: Superposed epoch analysis of nighttime disturbances. | 57 |
| Figure 4.4: SEA results for quiet nights..... | 61 |
| Figure 4.5: SEA of perturbations | 64 |
| Figure 4.6: Normalized SEA perturbations. | 67 |
| Figure 4.7: A sketch of particle precipitation spectra during E-region response phases. . | 71 |

List of Tables

| | Page |
|---|------|
| Table 2.1: Magnetometer stations used in AE derivation..... | 28 |

List of Abbreviations

- AC** – alternating code
- AE** – Auroral Electrojet
- AMISR** – Advanced Modular Incoherent Scatter Radar
- ASC** – all-sky camera
- CME** – coronal mass ejection
- CNA** – cosmic noise absorption
- CORS** – Continually Operating Reference Station
- COSPAR** – Committee on Space Research
- EEJ** – eastward electrojet
- Es** – sporadic E
- EISCAT** – European Incoherent Scatter radar
- EUV** – extreme ultraviolet radiation
- FoV** – field-of-view
- FUV** – far ultraviolet radiation
- GEONET** – GPS Earth Observation Network
- GPS** – Global Positioning System
- HF** – High Frequency
- hmE** – height of maximum electron density in the E-region
- hmF2** – height of maximum electron density in the F2-region
- IMF** – interplanetary magnetic field
- IPY** – International Polar Year
- IRI** – International Reference Ionosphere
- ISR** – incoherent scatter radar
- ITEC₁₅₀** – integrated total electron content to 150-km altitude
- KOD** – Kodiak SuperDARN radar
- LOS** – line-of-sight
- LP** – long pulse
- MLT** – magnetic local time

NGS – National Geodetic Survey

NmE – maximum electron density in the E-region

NmF2 – maximum electron density in the F2-region

PFISR – Poker Flat Incoherent Scatter Radar

RISR – Resolute Bay Incoherent Scatter Radar

SABER – Sounding of the Atmosphere using Broadband Emission Radiometry

SEA – superposed epoch analysis

SDI – Scanning Doppler Imager

SNR – signal-to-noise ratio

Sq – solar quiet

STARE – Scandinavian Twin Auroral Radar Experiment

STE – solar-terrestrial environment

SuperDARN – Super Dual Aurora Radar Network

SZA – solar zenith angle

TEC – total electron content

TECU – total electron content unit (10^{16} electrons per m^2)

TIMED – Thermosphere-Ionosphere-Mesosphere Energetics and Dynamics

URSI – International Union of Radio Science

UT – universal time

VHF – Very High Frequency

VLF – Very Low Frequency

WDC – World Data Center

WEJ – westward electrojet

Acknowledgements

First and foremost, I would like to thank my advisor Dr. Roman Makarevich for his constructive criticism, patience, and guidance during the research and writing of this thesis. The completion of this thesis would not have been possible without his invaluable input. I would also like to thank the members of my graduate committee – Dr. David Newman, Dr. Mark Conde, and Dr. Hui Zhang – for their support and for their insightful questions and advice, which helped me to consider my research from different perspectives.

A special thank you goes to my family. To Mom and Dad, I thank you for your continual support in every way you could manage (and then some). You helped me get through the rough patches even though you were thousands of miles away. I would not have even been able to come to UAF if it were not for you. To my sister Cynthia and her husband Matthew, I thank you for your words of advice and encouragement throughout my graduate education.

1. Introduction

1.1 Solar-Terrestrial Environment

Between the Earth and the Sun lies a region of space comprised of plasma primarily expelled from the Sun, as well as electric and magnetic fields which act on the charged particles of the plasma, and which, in turn, are modified by the plasma particles themselves. This system of particle-field interactions is what makes up the solar-terrestrial environment (STE). Effects of magnetic fields and field-particle interactions within the STE have been observed for centuries in the form of visible aurorae and movements of the compass needle. However, it is in the last hundred years that technological advances have allowed for more in-depth analysis of these phenomena. Moreover, in the last few decades, the number and variety of instruments taking data on the terrestrial end of the STE have created numerous opportunities to examine phenomena occurring in the STE using different diagnostic tools simultaneously.

On the far edge of the STE is the Sun. It progresses through cycles of activity, called the solar cycle, in which the Sun's magnetic field orientation changes with a period of approximately 22 years. Solar maxima mark the peaks of solar activity regardless of the Sun's field orientation and thus are separated by ~11 years. The ascending phase of the solar cycle is marked by an increase in the number of sunspots and solar flares, explosive events which send plasma toward the Earth. Sunspots have a lifespan of the order of 100 days, while the rotational period of the Sun is nearer to 28 days, which produces a shorter cycle of activity within the solar cycle as observed from the Earth.

Permeating the expanse outside the Sun's atmosphere is the solar wind. The solar wind is a combination of the fast-flowing plasma expelled by the solar corona and the solar magnetic field embedded into the plasma, called the interplanetary magnetic field (IMF). The solar wind plasma is composed primarily of protons and electrons, though it also contains a small percentage of other ionized particles such as fully-ionized helium or alpha particles. Near the Earth's orbit, the average density of both the protons and electrons is approximately 7 cm^{-3} and the plasma flows with speeds of ~400 km/s.

However, during periods of increased solar activity, events such as coronal mass ejections (CMEs) greatly increase both the solar wind velocity and the plasma density. Due to the rotational period of the Sun, the IMF radiates as a spiral connected to the Sun's surface, called the Parker Spiral [*Parker, 1958*]. Consequently, at the Earth's orbit, the direction of the IMF is at a $\sim 45^\circ$ angle to a line drawn straight between the Earth and the Sun.

On our side of the STE are the Earth and its geomagnetic field. The outermost region where the Earth's magnetic field controls the motion of particles is called the Earth's magnetosphere [*Hunsucker and Hargreaves, 2003*]. The portion of the magnetosphere that faces the Sun is compressed, while the opposite side takes a form of a long, comet-like tail, due to the solar wind pressure and interaction with the IMF. During events like CMEs and solar flares, the entire magnetosphere reconfigures, with one consequence being more channels through which the solar and magnetospheric particles can reach the Earth's atmosphere. Precipitating particles result in an increased auroral activity as well as in other changes in the terrestrial environment. Many of these changes can only be observed through their effects of technological infrastructure such as communication and power lines or using specialized equipment. Nevertheless, due to the humanity's ever-increasing reliance on this infrastructure, understanding of these phenomena, often referred collectively as Space Weather, is of paramount importance.

One important signature of Space Weather phenomena is magnetic effects. Early magnetic field measurements on the surface of the Earth recorded magnetic perturbations during increased solar and auroral activity. The close association of these magnetic effects with aurorae led to the first theories about electric field interactions occurring at high altitudes. The early radio experiments utilizing reflection of the radio waves from the atmosphere led to development of long-distance radio communication and to the discovery of the ionosphere, a region of the atmosphere containing ionized particles and electric currents that lies between the Earth and the magnetosphere. It is the ionosphere that is of primary concern to this thesis and as such it warrants a more thorough description.

1.2 The Earth's Ionosphere

The Earth's ionosphere is a region of the Earth's upper atmosphere that extends from approximately 50 km to 1000 km in altitude. Within the ionosphere, gases are ionized via processes such as photoionization and impact ionization, creating a plasma layer whose characteristics depend on many factors, including the Sun's elevation angle and level of activity. The ionosphere is subdivided into different layers, or regions, based on observed vertical profiles of various parameters such as the electron density and prevalent physical and chemical processes within each ionospheric region.

1.2.1 Ionospheric Regions

One of the key discoveries that led to an advent of the ionospheric physics discipline was that radio waves sent vertically into the atmosphere were reflected back to Earth rather than vanishing. From this, it was postulated independently by Kennelly and Heaviside that an electrically conducting ionosphere existed at some altitude surrounding the planet [*Kivelson and Russell, 1995*]. Later, three primary layers of the ionosphere were identified and named by *Appleton* [1930] based on the timing of arrival of reflected radio wave pulses. The first confirmed layer was named the E-region and the subsequently found layers were named D- and F- regions based on their vertical displacement from the first named layer.

Figure 1.1 shows a typical electron density profile of the ionosphere, with three ionospheric layers or regions marked. The electron densities plotted in Figure 1.1 were obtained from the International Reference Ionosphere (IRI) model [*Bilitza, 2008*] that was run for January 1, 2007 at geographic 65°N, 148°W at 0 UT (local midday) using an altitude step of 5 km starting from 60 km. The above location was highly representative of the auroral region in the Alaskan sector that is studied in this thesis.

The D-region is the lowest region of the ionosphere extending in height from approximately 50 km to 90 km. The D-region of the ionosphere requires the highest energy processes to cause ionization and thus has the lowest electron density out of the three regions. The primary process responsible for ionization is Lyman alpha radiation.

Electron densities in the D-region typically peak on the order of 10^3 electrons per cm^3 (10^9 per m^3) at the upper limits of the region's altitude.

The E-region is located between approximately 90 km and 150 km. Ionization in the E-region is mostly caused by soft X-ray and ultraviolet radiation. A typical maximum electron density in the E-region is $\sim 10^5$ electrons per cm^3 (10^{11} per m^3); it occurs during daytime while nighttime densities are considerably lower. However, a marked increase of electron density in the E-region during nighttime has also been observed. The increased nighttime electron densities can last anywhere from a span of minutes to hours. The reasons for this increase in nighttime electron density are of great interest for this thesis and as such, they are further discussed in Section 1.2.2.

The F-region is the highest region in altitude, residing above 150 km. The F-region is a broad region where photoionization by radiation with wavelengths between 20–90 nm plays the primary role. It is further subdivided into two separate layers: the F1 layer,

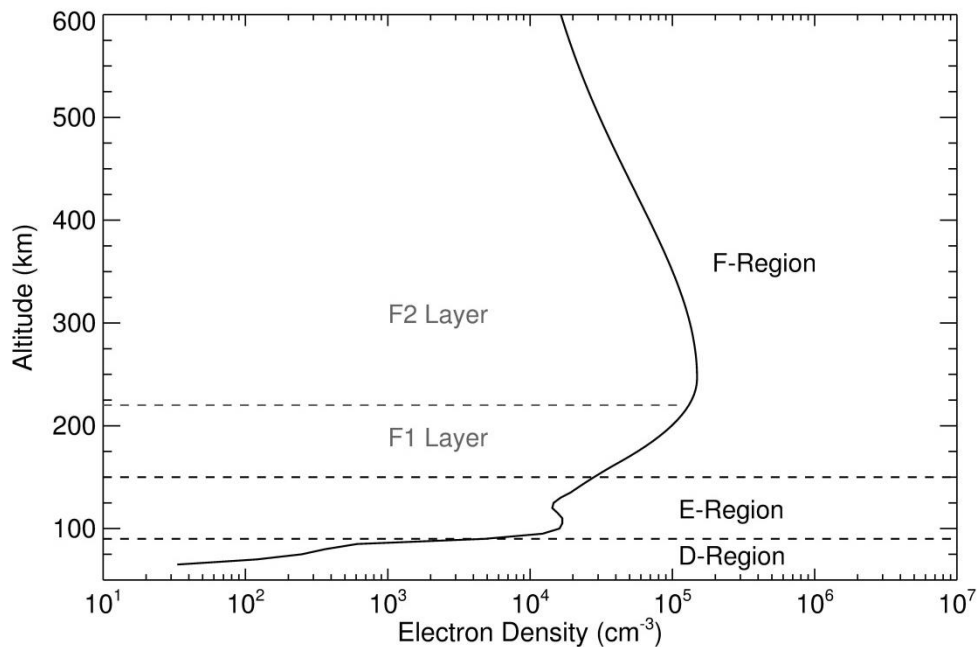


Figure 1.1: The three regions of the ionosphere. The D-region extends from roughly 50 km to 90 km, the E-region from 90 km to 150 km, and the F-region is the region above 150 km. The F-region is further split into two layers: the F1 layer, which extends to roughly 220 km, and the F2 layer, which is the region above 220 km.

which extends from 150 km to 220 km, and the F2 layer, which lies above 220 km, Figure 1.1. The main difference between them is that the F1 layer disappears at night. Typical electron densities in the F-region are approximately 10^5 per cm^3 (10^{11} per m^3) in the F1 layer and 10^6 per cm^3 (10^{12} per m^3) in the F2 layer. As the E-region, the F-region has a characteristic diurnal variation where the electron density increases after sunrise, reaches a peak during daylight hours, and decreases after sunset.

1.2.2 Ionospheric Electron Density: A Brief Survey of Past Observations

Variations in ionospheric electron density are of particular importance to this thesis and in this section, the normal, or average, behavior of electron density is discussed. Typically-observed values for electron density in various regions of the ionosphere were stated in the previous section. However, the electron density in any region of the ionosphere is constantly changing due to solar and other influences. The primary types of variations in electron density can be broken down into diurnal [*Mechtly and Smith, 1970; Coyne and Belrose, 1972*], seasonal [*Appleton and Naismith, 1935; Mechtly and Smith, 1968; Torr and Torr, 1973*], and solar cycle influences [*Beynon and Brown, 1959; Mechtly et al., 1972*].

In the following survey of past observations, the focus is on those specific studies that used the same type of instrumentation as that used in the present thesis, i.e. on the incoherent scatter radar (ISR) observations. Such observations are advantageous since they produce a full profile of ionospheric density, unlike ionosondes that can only produce a bottom side of the profile. In addition, the altitude resolution and accuracy is generally higher for ISR observations. Nevertheless, the summary of the past ionosonde observations is also given below, but it is presented in the form of the IRI model results, since IRI model is mainly based on this type of observations, particularly its earlier versions [*Bilitza, 1990*].

The most often observed variation in electron density is the daily increase in the E- and F-region densities during daytime. This diurnal variation is caused primarily by radiation from the Sun increasing the electron density by the process of photoionization in the two upper regions. As the solar zenith angle (SZA) changes with time of the day,

so does the ionization rate [*Chapman, 1931*], resulting in characteristic diurnal variation in the density.

Figure 1.2 shows the difference in the electron density at night (black) and day (grey) during solar minimum (dashed) and solar maximum (solid). The electron densities shown in this diagram were obtained from the IRI model, as described previously in Section 1.2.1. Solar maximum (minimum) conditions were simulated using a sunspot number of 200 (0). Similarly, daytime (nighttime) conditions were simulated by setting the local time to noon (midnight).

Figure 1.2 shows that in both parts of the solar cycle, the respective daytime electron densities are at least one order of magnitude greater than those at night in both the E- and F-regions, while there is little difference in the D-region.

A useful and well-documented measure of the electron content is the peak electron density in the F2 layer of the ionosphere and the height at which the peak occurs. Normally, these values are derived via the use of ionosondes and given the designations

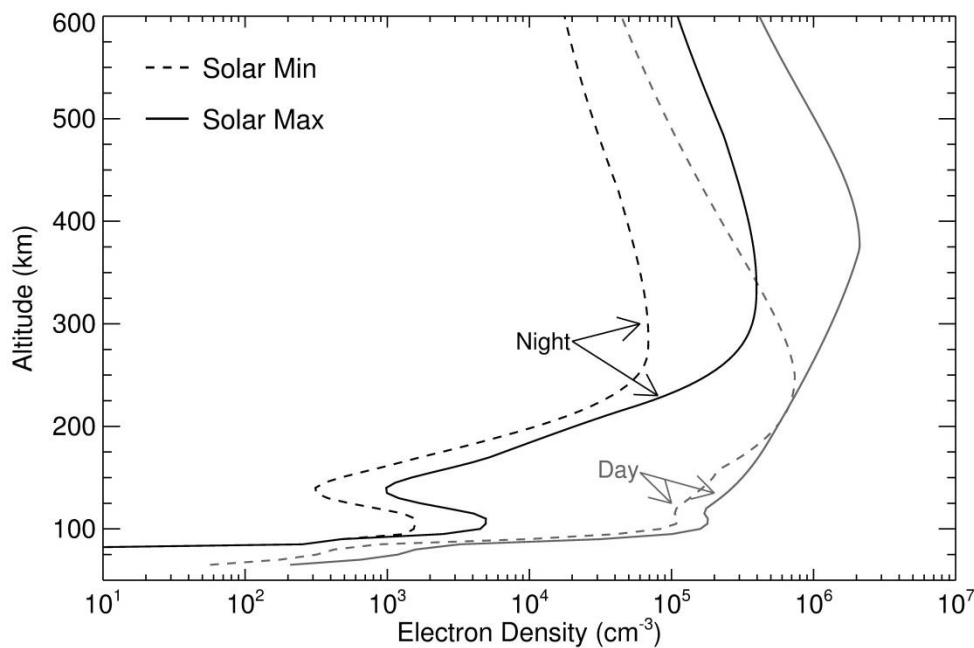


Figure 1.2: Electron density profiles under various conditions. Shown are the day- and nighttime electron densities during solar cycle maximum and minimum conditions. Daytime densities are greater than those during the night in all regions. During solar maximum, the electron density in the F2 layer at night exceeds that of the daytime solar minimum density in the same region.

NmF2 (peak density) and hmF2 (altitude of peak density) [Piggott and Rawer, 1978]. Similarly, ionosonde-derived E-region peak electron density and altitude of peak density are designated NmE and hmE, respectively. However, the peak electron density and altitude at which it occurs can be found using ISR systems as well. Even though the above terminology (NmF2, hmF2, NmE, and hmE) is normally reserved to ionosonde-derived values, for brevity sake the same notations will be used throughout this thesis to refer to the ISR-derived values as well.

Figure 1.3 illustrates the most salient features of the diurnal variation in the electron density; it presents measurements of electron densities on March 21, 2007 at various altitudes obtained with the Poker Flat ISR system near Fairbanks, Alaska (PFISR). The color scale is indicated on the right. PFISR is the primary instrument used in this thesis and details of its operations and technical capabilities are given in Section 2.1. For this

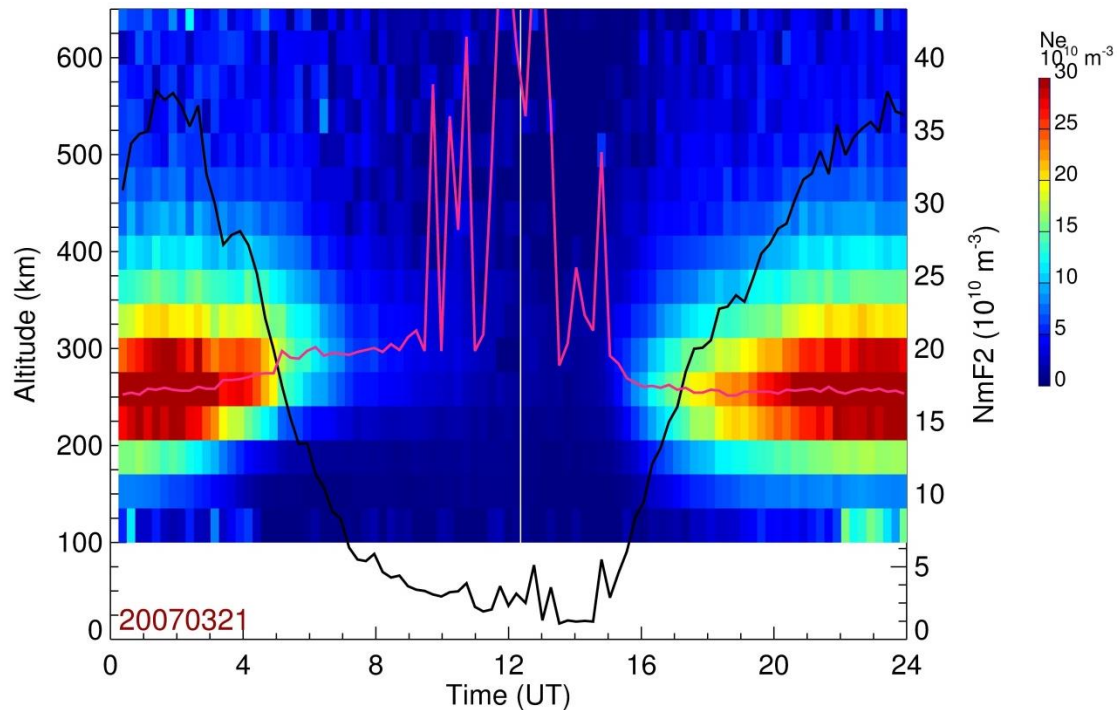


Figure 1.3: Diurnal variation of the electron density. Shown are measurements by the Poker Flat ISR system near Fairbanks, Alaska on March 21, 2007. ISR-derived hmF2 (pink line) reaches its lowest value during daytime hours (16-07 UT). ISR-derived NmF2 (black line) reaches a minimum late at night and a maximum near magnetic noon (23 UT).

example, the time resolution was 15 min and altitude resolution was 36 km.

The black (pink) line indicates the NmF2 (hmF2) throughout the day. In March, magnetic noon (magnetic local time or MLT of 12:00) is at ~23 UT. In Figure 1.3, this roughly coincides with the period where the increased F-region electron density has the largest extent in altitude. The greatest NmF2 value of the day occurs shortly afterward. Similarly, magnetic midnight (MLT of 00:00) is at ~11 UT. In Figure 1.3, this coincides with the period of the overall electron density trough. Likewise, the lowest NmF2 value of the day occurs near this time. The hmF2 value is reasonably stable during the daytime hours. It appears to reach the lowest altitude near magnetic noon (23 UT) and becomes highly fluctuating but trending toward much greater altitudes during the night.

In addition to solar photoionization, electron density is subject to local factors. In high-latitude regions, this includes the extent and activity of the auroral oval. Much of our early knowledge about density dynamics at these latitudes came from observations with the Chatanika radar, an ISR system which was operational on a campaign basis in the 1970s and which was located very close to the current location of PFISR. Using this radar and a nearby ionosonde, *Bates and Hunsucker* [1974] made observations under a variety of conditions ranging from quiet to very active. It was found that under quiet conditions the electron density profiles were not appreciably different from those observed at lower latitudes. In contrast, during periods of auroral activity, an extended layer of increased electron density near the E-region peak of 110 km was observed. An interesting, and important to the current study, feature of these observations was that this nighttime E layer was relatively thick (~30 km in vertical extent). This is in contrast with the more frequently discussed sporadic E (Es), a very thin layer of 1–2 km in altitude that is also commonly observed during the night [*Whitehead*, 1990]. Further observations of the E-region by *Hunsucker* [1975] also using the Chatanika radar showed that, in addition to the auroral activity, other phenomena, such as a total solar eclipse and auroral infrasonic waves, also have an impact on electron density. In particular, infrasonic waves can increase localized electron density on the same order of magnitude as auroral precipitation.

As mentioned, thin layers of electron density in the E-region, or sporadic E, have also been observed. The mechanisms behind these intensifications have been a point of research for a number of years, predominantly using ionosondes [Whitehead, 1970]. In the ISR era, *Turunen et al.* [1985] made use of high-resolution density measurements in the nighttime E-region using the European Incoherent Scatter (EISCAT) radar system in conjunction with electric field measurements from the Scandinavian Twin Auroral Radar Experiment (STARE) system of two coherent radars. Their aim was to investigate electric field compression as a potential cause of Es. They identified a layer structure that appeared at a low altitude during a time when the electric field switched to a northerly direction, as was theorized for field direction conditions for field compression in the Northern Hemisphere. This supported field compression of plasma as a possible mechanism of Es formation. In a more recent EISCAT study by *Turunen et al.* [1993], it was found that Es layers were almost always present in the E-region, without a particular peak in occurrence during the night, while a number of other structures were present in the E-region that exhibited diurnal behavior.

In addition to the diurnal variation, there are also seasonal variations in electron density, also attributable to the higher SZA during summer versus winter. The variations due to photoionization are the most extreme at high latitudes where there is nearly constant illumination at the peak of summer and little to no solar exposure at the peak of winter. The duration of the increased density follows the hours of sunlight and the intensity of the exposure. Thus in winter when there is the least amount of sunlight, the interval with enhanced density is the shortest. Also in winter, the Earth's rotational axis relative to the ecliptic is tilted, such that the slant path length for solar radiation to penetrate the atmosphere increases. This reduces the overall light intensity, which in turn means that the photons cannot penetrate as deeply and the lower regions of the ionosphere see very little increase in electron density. The reverse is true in summer. That is, when there are longer hours of more direct sunlight, the elevated electron density occurs for more hours in the day and there is enough photoionization occurring that the lower regions of the ionosphere experience a more consistent increase throughout the

day. In addition, seasonal effects may be associated with varying levels of geomagnetic activity that exhibits well-known equinoctial maxima. These maxima are a result of the increased probability that there will be a southward IMF component relative to the Earth's field near the vernal and autumnal equinoxes [*Russell and McPherron, 1973*]. During southward IMF, there is an increase in particle precipitation due to magnetic reconnection. These precipitating particles are the primary cause of impact ionization.

Both photo- and impact ionization mechanisms are affected by the solar cycle, Section 1.1. During the solar maximum the electron density in all the regions of the ionosphere increases due to greater photon flux. However, it is the F2 region and topside of the ionosphere that have the greatest density increase during the solar maximum. In Figure 1.2, the average night- and daytime electron densities were shown for both solar minimum and solar maximum. In the E- and D-regions of the ionosphere, the electron density for the same time of day is greater during solar maximum. The largest difference between solar minimum and solar maximum in the lower layers occurs during the night. In contrast, for the F-region, both night- and daytime electron densities are noticeably greater during solar maximum. Electron density at night in the F2 region during solar maximum actually exceeds that during the day during solar minimum. The solar cycle effects are more direct on the dayside, but they also exist and in fact are very significant during the night.

1.2.3 Ionospheric Current Systems

The forecasting of aurora and the associated density enhancements in the nighttime E-region can be made by looking for perturbations in the Earth's magnetic field. Magnetic perturbations can be observed using global indices, such as the Auroral Electrojet (AE) index in the northern auroral zone, Section 2.2.2, and the Kp index derived from sub-auroral stations. The perturbations measured by instruments to derive the various geomagnetic indices are related to electrical currents and their behavior as described below.

The ionosphere is a dynamic environment containing several current systems that also couple the ionosphere to the magnetosphere. Depending on the direction, the

currents are classified as Pedersen, Hall, or Birkeland currents. Pedersen currents flow perpendicular to the magnetic field and parallel to the electric field, Hall currents flow perpendicular to both magnetic and electric fields, and Birkeland currents are parallel to the magnetic field. From these, two major current systems are formed in the ionosphere: the equatorial electrojet and the auroral electrojet.

The equatorial electrojet, as the name implies, forms in the region on either side of the magnetic dip equator with the northern (southern) portion flowing in a counterclockwise (clockwise) direction, as shown in Figure 1.4a. The equatorial electrojet is an east-west current system which forms on the dayside of the Earth, also called the solar quiet (Sq) current system. It is a dynamo primarily driven by the Hall currents and restricted to a region between 90–160 km in altitude, i.e. the E-region [Forbes, 1981].

The auroral electrojet is formed in the auroral zone. It consists of eastward (18–00 MLT) and westward (00–06 MLT) electrojet components (EEJ and WEJ in Figure 1.4b). Similarly to the equatorial electrojet, the auroral system is a set of Hall currents which cross Pedersen currents (red) extending over the polar cap and auroral zone. The

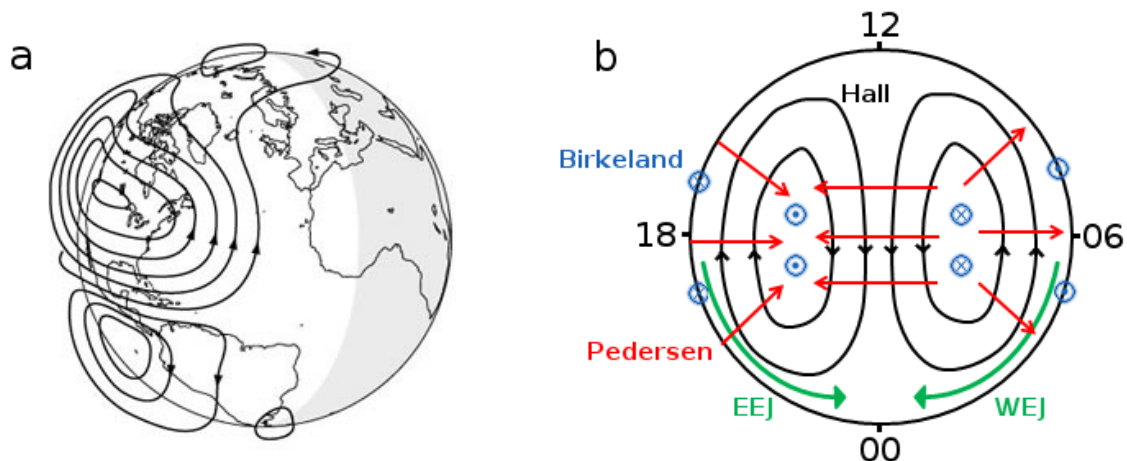


Figure 1.4: Major ionospheric current systems. The equatorial electrojet (a) is an east-west current system present on the dayside of the planet, centered around the magnetic dip equator. The auroral electrojet (b) is a current system in the nightside auroral region consisting of an eastward (EEJ) and westward (WEJ) component. The strength of auroral electrojet system is indicative of auroral and substorm activity. Panel (b) shows the Northern Hemisphere from the north magnetic pole, down to 60° magnetic latitude. Figure 1.4a is taken from U.S. Geological Survey Web site: www.usgs.gov.

black lines show the ionospheric convection streamlines. In the E-region, the ions are controlled by collisions with neutral particles and hence are largely stationary, while electrons are magnetically-controlled and move with background convection. Thus, the conventional currents (flow of positive charges) in the nightside E-region are as shown by the green arrows. Birkeland currents (blue) connect the electrojet system to the magnetosphere. The intensity of the auroral electrojet is related to activity in the auroral region. During quiet periods the strength of the auroral current system is low, while during periods of activity, such as substorms, the strength of the current system, especially that in the westward electrojet, increases. The measure of the intensity of the auroral electrojets, thus, can be used as an indicator of activity in the auroral zone. The system of measurement of the auroral currents is called the AE index; it is described in greater detail in Section 2.2.2.

1.3 Observational Techniques and Models

Observations of auroral phenomena and E-region electron density have been made with a variety of instruments over the past several decades. Each type of instrumentation has brought new information about the behavior of the E-region. Some of the more recent techniques are briefly discussed in the following sections along with models based on data acquired from them.

1.3.1 Coherent Radar Observations of Plasma Irregularities

Coherent scatter radars, or simply coherent radars, have been in use since the early 1950s, though the first observations of this type of scattering were made in 1926. The purpose of coherent scatter systems is to probe the ionosphere for field-aligned irregularities generated by plasma instabilities [*Hunsucker and Hargreaves, 2003*]. To receive coherent scatter from plasma density irregularities propagating in the ionosphere, the irregularity wave number must be twice that of the radio wave. This means that a coherent radar operating at a particular frequency (which is the vast majority of the past or current coherent radar systems) would only detect irregularities of a particular scale or wavelength. In addition, as irregularities are formed along magnetic field lines, in order

for coherent backscatter to occur, the radar's line of sight must be nearly perpendicular to the magnetic field [Schlegel, 1995].

Most coherent scatter systems operate in the Very High Frequency (30–300 MHz; VHF) or High Frequency (3–30 MHz; HF) range, although Very Low Frequency (VLF) radars have also been used in the exploration of the D- and E-regions of the ionosphere at higher latitudes. One example of coherent radar operations at HF is the Super Dual Auroral Radar Network (SuperDARN): a network of coherent radar systems operating around both poles. SuperDARN has been instrumental in the study of convection patterns in the ionosphere under various IMF conditions [Ruohoniemi and Greenwald, 1996; Kustov *et al.*, 1997; Bristow *et al.*, 1998; Baker *et al.*, 2007]. SuperDARN has also played an important role in research into meteor trail echoes, which can be used to determine neutral atmosphere dynamics [Hall *et al.*, 1997; Jenkins *et al.*, 1998; Bristow *et al.*, 1999; Chisham and Freeman, 2013]. While coherent radars do not measure electron density directly, a lot of useful information about density distribution can be obtained from analysis of irregularity power – and to some extent its velocity and width – since it is the electron density that is responsible for bringing the radar beam to the orthogonality with the magnetic field line, a condition for peak coherent power.

1.3.2 Incoherent Radar Measurements of Plasma Parameters

The first experimental use of incoherent scatter radar in observations of the ionosphere occurred in 1958. At that time, the proposed theory for what the ISR signal return would look like relied only on the properties of electrons in the ionosphere; thus, it was expected that the power return would be several orders of magnitude smaller than what was possible with coherent scatter systems and the spectrum of the signal would cover a bandwidth of several hundred kHz. While the power of the signal came as expected during the first experiments, the spectrum was much narrower [Evans, 1969]. From those results, it was deduced that ions had a larger impact on the behavior of the signal.

Although the small power return in ISR systems makes it more difficult to extract a signal spectrum from the noise, the ISR return signal contains information about

background ionospheric plasma itself rather than about plasma irregularities that coherent scatter radars observe. Electron density, electron to ion temperature ratio, ion temperature to mass ratio, and line-of-sight (LOS) plasma velocity are directly measured, Section 2.1, while neutral properties and conductivities can be also derived from the measurements [Beynon and Williams, 1978]. These measurable variables yield an excellent description of ionospheric properties and dynamics, making ISR a powerful observational tool.

ISR systems that are currently operational are located across the globe including previously mentioned EISCAT in Scandinavia and PFISR in Alaska. Other ISR facilities include the Jicamarca radar in Peru, the Arecibo radar in Puerto Rico, the Millstone Hill radar on the East coast of the US, the Irkutsk radar in Russia, the Sondrestrom radar in Greenland (previously stationed in Chatanika, Alaska), and the Resolute Bay ISR in the Canadian Arctic (RISR). ISR systems have been used in the investigation of numerous phenomena including sporadic-E layers at various latitudes [Miller and Smith, 1975; 1978; Huuskonen *et al.*, 1988; Nygrén, 1989] and thermospheric wind dynamics [Salah and Holt, 1974; Wand, 1983; Griffin *et al.*, 2004].

1.3.3 GPS TEC Measurements

Historically, the use of satellites to make studies of the Earth's ionosphere began with observations of the orbit of the very first satellite leading to information about air density [e.g., see for early satellite research the review paper by Willmore, 1974]. Subsequently, satellite exploration of the magnetosphere and ionosphere yielded more information about the upper atmosphere. The Global Positioning System (GPS) consists of a system of satellites in medium-Earth-orbit such that a given location on the surface of the planet is in LOS of several satellites at all times. The network offers the opportunity to investigate properties of the ionosphere in multiple locations across the globe with thousands of receiver stations. Typically, somewhere between six and eleven satellites are visible across a station at any given time [Parkinson and Spilker, 1996].

GPS was first conceived in the early 1970s and put into full use in the mid-1990s. Satellites broadcast at two different frequencies: 1575.42 MHz (called L1) and 1227.60 MHz (L2). Electromagnetic waves traveling through the ionosphere have a time delay

that depends on the frequency of the wave and is proportional to the number of electrons along the path of travel. Thus, by tracking the time delay of the signals transmitted by the satellites, it is possible to determine the total electron content (TEC) along the path of travel of the signal [*Parkinson and Spilker, 1996*].

There are several GPS receiver networks operating currently. The Continually Operating Reference Station (CORS) is a network of over 1800 receivers, primarily based in the US and its territories, managed by the National Geodetic Survey (NGS). The GPS Earth Observation Network (GEONET) consists of over 1000 receivers in Japan, operated by the Geophysical Survey Institute. In Europe, there are over 800 receiver stations managed by scientific organizations in their respective countries.

The wide latitudinal coverage available in the global GPS receiver network makes it a highly versatile system for ionospheric studies, though the measurements of TEC under various conditions is the primary use of GPS in ionospheric studies. While ISRs are capable of determining electron content, they do so by integrating a density profile, which ends at the maximum viewable height of the particular ISR (e.g. ~660 km for PFISR). GPS, on the other hand, measures a *total* electron content, which includes contributions from altitudes beyond the altitude range of ISRs. However, both types of instruments have good coverage of the F-region, where the majority of the contribution to TEC comes from. Thus, GPS and ISR electron content measurements generally have a good agreement [*Makarevich and Nicolls, 2013*].

1.3.4 TIMED-SABER Measurements of E-region Density

The Thermosphere-Ionosphere-Mesosphere Energetics and Dynamics (TIMED) satellite is designed to study the dynamics of the atmosphere approximately in the altitude of the E-region. It has several instruments on board, including the Sounding of the Atmosphere using Broadband Emission Radiometry (SABER) instrument. SABER is designed to measure a wide spectral range to investigate temperature dynamics in the atmosphere.

Using the spectral measurement capabilities of SABER to measure the volume emission rates of NO^+ ions, *Mertens et al.* [2013] studied emissions from the auroral

ovals to come up with a model for E-region electron density during storm periods. They used NO^+ as a proxy for electron density as it is one of the most prevalent ions in the E-region, thus by the neutral-charge nature of plasma, the electron density would closely follow. Observations from SABER showed that during periods of high geomagnetic activity, NO^+ emissions near and below 60° latitude in either hemisphere were greatly enhanced. The TIMED-SABER measurements of nighttime E-region density have been used to improve ionospheric models as described below.

1.3.5 IRI and STORM-E Models

The International Reference Ionosphere (IRI) is a widely used model developed by the Committee on Space Research (COSPAR) and the International Union of Radio Science (URSI) [Bilitza, 2001]. IRI is based on experimental data obtained from various ground- and space-based instrumentation, with the earlier models being largely based on ionosonde measurements. The model allows for numerous input parameters – including but not limited to height resolution and range, time (local or universal), latitude and longitude, and solar conditions – which are used to generate an ionospheric profile of desired values such as electron density, plasma drift, ion, electron, and neutral temperatures, and TEC. Optional input parameters such as solar conditions that are not specified by the user are determined by a running average of acquired data [Bilitza, 2001]. As mentioned in Section 1.2.2, the IRI model output for the electron density was used in Figures 1.1 and 1.2.

The IRI model has been updated several times since its inception. In particular, electron density profiles have undergone numerous adjustments in the last decade. In IRI 2000, D-region density profiles were improved with the inclusion of more rocketry data, E-region density modeling was updated with a variety of ISR-derived data, and F-region density profiles received the most extensive updates with improved databases and profiling models for different altitudes within and above the F-region during both quiet and active geomagnetic conditions [Bilitza, 2001]. In IRI 2007, E-region electron density profiles received further updates for higher latitudes with data from EISCAT and rocket experiments [Bilitza and Reinisch, 2008].

Despite the improvements to E-region profiles in prior updates, *Mertens et al.* [2013] showed that IRI-generated electron density profiles at auroral latitudes during storm conditions were still underestimating density. *Mertens et al.* [2013] developed an adjustment model, called STORM-E, based on satellite and ISR readings in the auroral region to better account for ionization due to auroral particle precipitation. For auroral latitudes, STORM-E generated electron density profiles compared well with ISR-gathered data with great improvement on the prior IRI model. The STORM-E adjustment was included in the most recent release of the IRI model: IRI 2012 [*Mertens et al.* 2013].

1.4 Motivation, Aims, and Objectives

As industry and society has become progressively reliant on electrical grids, satellites, computers, and other complex networks, the impact of the ionosphere on human way of life has become increasingly important. Long-distance communication and satellite navigation rely on the propagation of radio signals through the ionosphere, with the ionospheric plasma playing a critical role in controlling this propagation. Thus, the better our understanding of the processes within the ionosphere is, the better prepared we can be to deal with their influences on technology.

The ionospheric electron density has been investigated for a number of years using a variety of methods, as was discussed in Section 1.2.2. The nighttime E-region in particular has been a point of interest due to phenomena such as auroral particle precipitation and sporadic-E, both of which can have a drastic effect on radio wave propagation. Most of these previous studies however, focused on case studies and on thin Es layers. In contrast, statistical behavior of thick layers of ionization near 110 km associated with aurora remains significantly less investigated. For example, the behavior of the electron content of the E-region with respect to geomagnetic and auroral activity or seasonal factors is not yet fully understood. Similarly, the typical behavior of the full profile of ionospheric density within the E-region versus time during auroral events remains largely unknown. One reason for these gaps in our knowledge is the lack of continuous monitoring of the nighttime E-region. Empirical models of the ionosphere,

such as the IRI, can be used to approximate E-region conditions when observations are not available. However, some improvement is still desired in performance of these models, particularly in the high-latitude region, where ISR observations often exhibit significant disagreements with the IRI model predictions during geomagnetic disturbances such as storms, Section 1.3.5. PFISR is the most recently completed ISR facility in the auroral region and as such, PFISR observations are largely not included into IRI. Unlike its predecessors, including Chatanika ISR in Alaska, PFISR has operated on nearly continuous basis since its deployment in 2007. Thus, data collected by PFISR can be used to greatly improve the accuracy of existing models of the ionosphere.

This thesis contributes to this effort of improving our knowledge of nighttime E-region dynamics. In particular, this thesis aims to investigate the behavior of E-region electron density during nighttime geomagnetic disturbances using data from PFISR and magnetometers in the auroral region. Section 2 describes the instrumentation utilized in this research focusing on the ISR technique and specifics of PFISR operations and data processing. Section 3 presents results from the first original research project, in which the relationship between E-region electron content and auroral activity is investigated utilizing an extensive dataset collected by PFISR. The specific objectives of this project are (1) to evaluate the extent to which the E-region electron content is controlled by auroral activity, (2) to investigate factors that may influence this control such as diurnal and seasonal dependencies, and (3) to estimate the contribution that the E-region makes to the TEC of the ionosphere and study its dynamics. Section 4 presents results from the second original research project that focuses on the superposed epoch analysis of the E-region electron density versus time from onset of auroral disturbance. The specific objectives of this project are (1) to statistically investigate the behavior of the full electron density profile throughout auroral disturbances, (2) to characterize behavior of thick auroral E layers using ISR-derived NmE and hmE values, and (3) to analyze the evolution of auroral particle precipitation spectra during auroral disturbances.

2. Instrumentation

In this thesis, two types of instrumentation were used to investigate the ionosphere in the auroral zone: incoherent scatter radar and magnetometers. The following sections describe these two types of instrumentation and the principles behind their operation, starting with the incoherent scatter technique in Section 2.1 and followed by magnetometry in Section 2.2.

2.1 Incoherent Scatter Radar

The basics of the ISR technique were presented in Section 1.3.2. Here more details on the ISR technique and data processing are presented, with particular focus on PFISR, the principal instrument used in this thesis. Incoherent scatter radar is a powerful tool for measuring several ionospheric properties in the E- and F-regions. The term “incoherent” scatter arises from the random thermal motion of electrons present in the ionosphere, which causes radio signal scattering over a range of Doppler shifts seen by the radar receiver as varying signal power over a spectrum of frequencies. However, as explained below, the signals that ISR systems work with are not from individual electrons, but from ions arranged in structures that in many ways behave coherently. Nevertheless, the term “incoherent” is widely used to distinguish from coherent scatter technique that utilizes much larger and much more coherent structures, Section 1.3.1.

2.1.1 Incoherent Scatter Principles

The scattering of electromagnetic waves by single electrons was first studied by Thomson in the early 1900s. He determined that the energy scattered by an electron into solid angle per incident flux is given by $(r_e \sin \phi)^2$ where r_e is the classical radius of an electron and ϕ is the polarization angle. It is by convention of radar operation that the target is assumed to behave as a perfectly conducting sphere in scattering energy; thus, the cross section of an electron can be written as:

$$\sigma_e = 4\pi(r_e \sin\phi)^2 \approx 10^{-28} \sin^2 \phi [m^2]. \quad (2.1)$$

Gordon [1958] first proposed the use of incoherent scatter radar as a tool for investigating the Earth’s ionosphere. He postulated that the scattering cross section for a volume of N electrons is given by $\sigma_n = N\sigma_e$, which was later shown by *Fejer* [1960] to be

true for small wavelengths of radio waves in a gas at thermal equilibrium. The “small” wavelength to which he referred was in relation to the Debye length of the plasma. The Debye length defines the shielding distance surrounding a charged particle in a plasma. For most ionospheric conditions, the Debye length is less than 2 cm.

As indicated by *Fejer* [1960], the size of the probing wavelength relative to the Debye length of the electrons observed in the ionosphere is an important factor to consider. *Buneman* [1962] showed that the effective cross section for incoherent scatter can be given by:

$$\sigma = \frac{\sigma_e}{(1 + \alpha^2)(1 + T_e/T_i + \alpha^2)} \quad (2.2)$$

where $\alpha = 4\pi D/\lambda$, with D representing the Debye length and λ the exploring wavelength. At lengths much smaller than the Debye length, plasmas are no longer capable of organized motion; thus probing the ionosphere with a wavelength much smaller than the Debye length will yield observations of the electrons undisturbed by plasma interactions. The use of a wavelength smaller than the Debye length will yield a scattering cross section for a volume of electrons as predicted by *Gordon* [1958]; i.e. $\sigma_n = N\sigma_e$. However, in practice, the wavelengths used in radar observations of the ionosphere are on the order of 1 m, which is much larger than the Debye length. For example, PFISR used a frequency of 450 MHz, which corresponds to the wavelength of ~67 cm. In the scenario where the observation wavelength is much greater than the Debye length, the scattered radio signal received by the radar is no longer due to individual electrons. Rather, it is due to fluctuations of the electron density in the observed plasma region due primarily to ion acoustic waves. The effect of ion acoustic waves on scattering is to narrow the frequency spectrum received compared to the expected spectrum caused by the “true” incoherent scatter, i.e. due to solely electrons, as was first observed by *Bowles* [1958]. In effect, the presence of ion acoustic wave interactions introduces a degree of coherence to the scattering such that wholly incoherent scatter is not achieved.

Figure 2.1 shows an idealized incoherent scatter spectrum dominated by broadening due to ion acoustic waves around what is called the ion line (shown in green). One should

note that even though this spectral broadening is still present, it is still much smaller than that expected for the “truly” incoherent scatter. Another sharp, narrow-band echo corresponding to the plasma frequency, called the plasma line, appears as a result of Langmuir waves (shown in orange). The plasma line appears as both an upshifted and downshifted line from the ion line and is the most prevalent when electrons are hot. While both the plasma and ion lines can be used to determine properties of the ionosphere, it is the ion line spectrum that is utilized the most in the ISR technique.

2.1.2 Data Processing/Spectrum Analysis

The shape of the spectrum and strength of the return echo from incoherent scatter can be used to determine a number of properties of ionospheric plasma as detailed below. Most properties can be determined directly from the return echo with careful processing. Of primary interest to this thesis is the determination of the electron number density which is derived from the total power of the return echo (the green area in Figure 2.1).

Evans [1969] showed that the power received by the radar is related to the electron

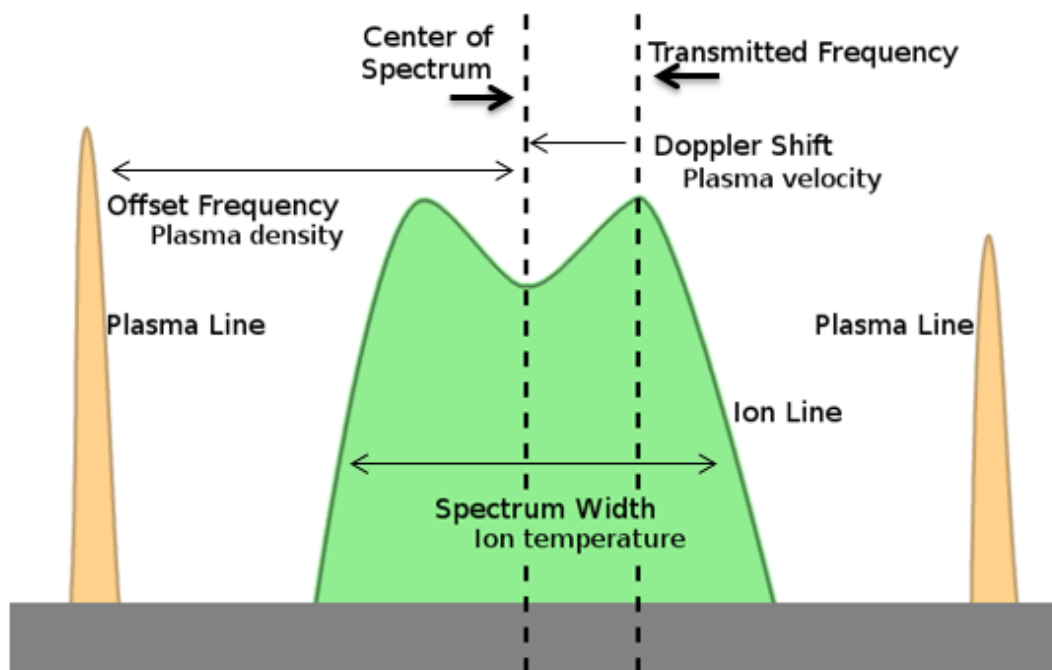


Figure 2.1: Example of incoherent scatter signal spectrum. Both ion and plasma lines are shown. Frequency increases to the right and power is represented by the height of the ion and plasma lines. See text for details on signal processing and ionospheric parameters derived.

density, radar cross section, and height by:

$$P_S(h) = C \frac{N(h)\sigma(h)}{h^2} \quad (2.3)$$

where C is a proportionality constant which can be determined from calibration, h is the height, $N(h)$ is the height-dependent electron density profile, and $\sigma(h)$ is the effective radar cross-section given by Eq. (2.2). The cross-section profile $\sigma(h)$ has a dependence on the electron to ion temperature ratio as well as on the parameter α through Eq. (2.2).

As was discussed in Section 2.1.1, the ISR systems use the probing wavelength λ that is much greater than the Debye length D (typically 1 m vs. 2 cm). In this case, $\alpha = 4\pi D/\lambda \rightarrow 0$ and can be ignored, leaving only the temperature ratio to determine. The temperature ratio is determined for each altitude by analysis of the return spectrum, where the peak-to-valley ratio in the ion line characterizes the temperature ratio, Figure 2.1. Once this ratio is determined, the electron density is found by rearranging Eq. (2.3) and finding constant C from calibration using either coincident density measurements by some other instrument (e.g. ionosonde) or by using the plasma line (the orange area in Figure 2.1) offset from the center of the spectrum to determine the plasma frequency. The plasma frequency is related to the electron density through:

$$\omega_p^2 = \frac{N e^2}{\epsilon_0 m} \quad (2.4)$$

where N is the electron density, e is the elementary charge, ϵ_0 is the permittivity of free space, and m is the mass of an electron.

The other plasma parameters that can be determined from the ion line spectrum are the electron and ion temperature, average ion mass (with some aid from a model), and LOS ion velocity. Thus, the height of the peaks of the ion line spectrum determines the electron temperature, where hotter electrons create sharper peaks.

The width of the ion line lends information about the ionic composition of the atmosphere probed. Variations in both the average mass and temperature of the ions change the width of the spectrum; ions that are lower in mass or higher in temperature can increase the width, while lower temperature and higher mass ions decrease the width. In principle, it is not possible to determine either the ion mass or temperature from the

spectrum width without knowledge of what the other parameter is. Nevertheless, information about chemical composition and hence about the average ion mass can be taken from a model, and thus the ion temperature is possible to derive.

The Doppler shift of the frequency of the spectrum, i.e. the difference between the transmitted frequency and the center of the return spectrum frequency, Figure 2.1, yields the plasma velocity along the LOS of the radar. If the ions and electrons are moving together, the shape of the spectrum will be symmetrical. If, on the other hand, one is moving relative to the other, the power peaks on either side of the spectrum center will become asymmetrical.

2.1.3 Poker Flat Incoherent Scatter Radar

The Poker Flat Incoherent Scatter Radar, or PFISR, located at the Poker Flat Research Range (65.13°N, 147.47°W) near Fairbanks, Alaska (Figure 2.2) is a phased array system consisting of 4,096 antennae across 128 panels designed to probe the ionospheric plasma [*Heinselman and Nicolls, 2008*]. PFISR is a new-generation ISR system based on the Advanced Modular ISR (AMISR) design. AMISR systems are able to steer electronically rather than mechanically by adjusting the phase difference between antennas to enforce signal propagation in the desired direction. The capability of steering electronically is advantageous since the radar steers on a pulse-to-pulse basis, which allows for the resolving of spatial and temporal ambiguities that are characteristic of mechanical radar dishes. PFISR is oriented such that the boresight has an elevation angle of 74° and an azimuth angle of 15° (east of geographic north), Figure 2.2. It has over 400 preprogrammed look directions, though it is capable of steering to any look direction within the limits of its sight (shown by the yellow contour in Figure 2.2). Figure 2.2 shows 3 of these preprogrammed look directions or beams by the pink lines (to an altitude of 350 km).

PFISR is typically operated in two primary modes: a low-duty cycle mode and a higher power mode for specialized experiments. The important advantage of AMISR systems is that they are capable of running continuously in the low-duty cycle mode. This is mainly because, unlike large dish systems, AMISR systems do not have moving

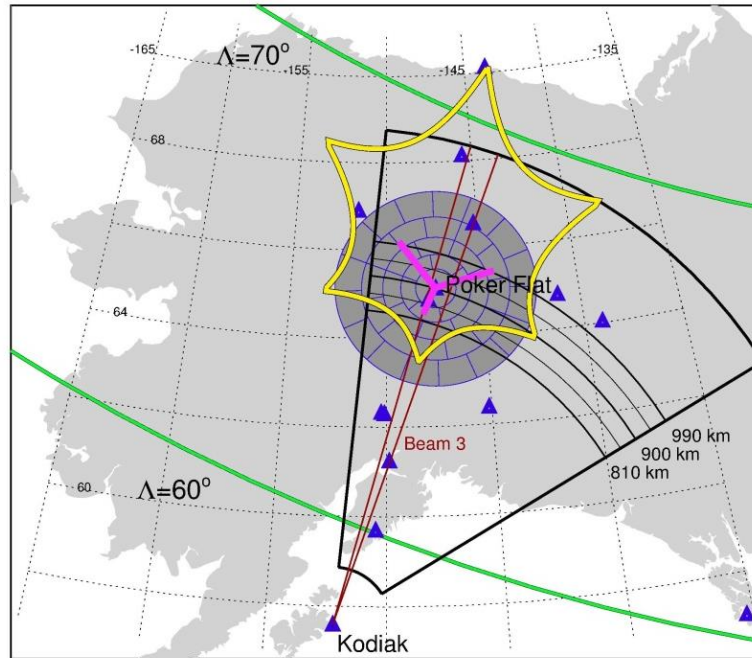


Figure 2.2: PFISR and local instrumentation around Poker Flat. Blue triangles represent nearby magnetometer stations. Yellow outline indicates PFISR field-of-view (FoV) at a 400-km altitude. Pink lines represent three of the possible look directions of PFISR. Blue outlined, dark grey concentric circles indicate the FoV of Scanning Doppler Imager (SDI) out to zone five. Black outline indicates the FoV of the SuperDARN coherent HF radar at Kodiak (KOD) to a slant range 1215 km. The three other selected ranges are shown by the black circular lines. Beam 3 of KOD is highlighted. Green lines represent lines of equal magnetic latitudes 60°N and 70°N.

parts and as such can operate unattended. PFISR started its routine operations in March 2007 during the International Polar Year (IPY) and for most of the time since then, PFISR operated on a continuous basis in the low-duty cycle mode collecting the data from 1–4 beams, one of which is usually along the local magnetic field line (equatorward-directed beam in Figure 2.2). The electron density data in this thesis are from this field-aligned beam (beam 64157 in the PFISR numeration scheme). After the end of the 18-month IPY period, PFISR continued to operate in IPY-compatible modes when not in use for other observations.

PFISR, like other ISR systems, normally collects raw data at 5-10 s intervals. To increase the signal-to-noise ratio (SNR), the raw data is post-integrated and analyzed. During analysis, various ionospheric parameters are derived as described in the previous

section. Although post-integration periods can be chosen differently, often limitations are imposed by the ionospheric conditions, particularly during the descending phase of the solar cycle and particularly for low-duty-cycle IPY modes. Thus, the post-integration period for the IPY dataset considered in this thesis was 15 min, which placed a limit on time resolution for this thesis. Nevertheless, the nearly-continuous data collection during IPY mode operations provided electron densities throughout all seasons during a variety of conditions, allowing the opportunity in this thesis to investigate electron density dynamics in context of a wide range of factors.

While in IPY operations, PFISR uses two pulse types to probe the ionosphere: a long pulse (LP) mode designed for the F-region studies, and an alternating code pulse (AC) designed for probing the E-region. The AC pulse mode, as described by *Farley* [1969] and *Lehtinen and Häggström* [1987], is a multi-pulse transmission technique where the phase of the pulses within a group is switched in a specific pattern. By employing an AC technique, greater spatial resolution is achieved, allowing for greater detail in the lower-altitude regions of the ionosphere. In the F-region, the LP method yields better data, but at the cost of range resolution. PFISR AC mode yields a resolution of 4.5 km, while the LP mode yields a 72 km range resolution.

Finally, Figure 2.2 shows that PFISR has an excellent complement of other instruments that are capable of providing coincident data in space and in time, since many of them also operate in near-continuous regime. The three examples of these instruments are the SuperDARN Kodiak radar (KOD), the Scanning Doppler Imager (SDI), and the all-sky camera (ASC). KOD is a coherent scatter radar which is oriented such that its FoV overlaps PFISR, with beam 3 passing directly overhead of Poker Flat and being aligned with beam 64157 of PFISR. The SuperDARN radars, including KOD, measure properties of field-aligned plasma irregularities, such as their LOS velocity, in the E- and F-regions, as was described in Section 1.3.1. The SDI is a high-resolution optical spectrometer used to measure Doppler broadening and Doppler shifts of aurora and airglow emissions [*Conde and Smith*, 1997]. The ASC photographs the night sky,

observing characteristics of aurorae such as their development, emission spectrum, and fine structures.

A systematic study that would involve these datasets in addition to PFISR measurements is well outside the scope of this thesis. Here the focus is on PFISR and IPY data collected in 2007–2010. The reasons for this selection are as follows. First, it provides an excellent opportunity to investigate electron density dynamics during extreme solar cycle minima such as that following the solar cycle 23. Second, it serves as a complementary analysis to a study by *Makarevich and Nicolls* [2013] which compared PFISR- and GPS-derived TEC for the same years. While comparing PFISR- and GPS-derived TEC, their study effectively considered the contribution of electron content in the PFISR observed region (~100–660 km) to the full TEC profile (0–20,200 km). Similarly, this thesis considers the contribution of the E-region (~80–150 km) to PFISR-derived TEC. Third, magnetometer data, which was used as a proxy for auroral activity as described in the following section, was continuously available during this period.

2.2 Magnetometry

Magnetometry is the use of instrumentation to measure magnetic fields, such as that of the Earth. The two types of ground-based devices that are commonly used in geophysics research are the fluxgate magnetometer and the induction coil magnetometer. The former is used predominantly to measure magnetic field perturbations due to the current systems in the ionosphere (and, to some extent, in the ground). The latter are used to measure the rate of change in the magnetic field. Since most geomagnetic indices – including the AE index that is employed in this thesis – utilize fluxgate magnetometer measurements, its principles of operation are described next.

2.2.1 Fluxgate Magnetometer

Due to its durability and reliability, the most commonly used type of magnetometer for obtaining readings of the Earth's magnetic field is the fluxgate magnetometer. Fluxgate magnetometers are used in ground-based magnetic stations where fluctuations of the Earth's magnetic field must be measured against a steady background field of

roughly 60,000 nT. Fluxgate magnetometers are also used on low-Earth orbit and deep-space satellites where field orientation with respect to the craft varies and where sensitivities of a few nanoTesla are required. There are several different designs of fluxgate magnetometers, ranging from single core to two-axis ring core, reflecting their intended operational use. *Gordon and Brown [1972]* describe the different possibilities of design configuration as follows.

Early designs of magnetometer intended for geophysical research used a magnetizing field oriented parallel to the external field. This “parallel” variety of magnetometers is still the most commonly used type of fluxgate magnetometer, but a second type using a field perpendicular to the background field was also developed. The “perpendicular” variety differs from the parallel variety in that only one core is required. While a single core is possible in the parallel type, the unbalanced flux in the system can be problematic.

Additionally, magnetometer designs vary to create single- or multi-axial devices. Single-axis designs are only capable of measuring one component of the external magnetic field, while two-axis and three-axis designs are used for a more thorough analysis of the local field, including derivation of the magnetic dip angle. Ring cores of the parallel type can be set up as either a single- or a two-axis device and are most useful in low-noise sensors.

All variations of the fluxgate magnetometer operate on the same basic principles, though different core designs use alternate approaches. The core of the magnetometer is a high permeability material wrapped in a wire pick-up coil and a driving coil. A high frequency alternating current is passed through the driving coil, which saturates the core on half cycles of the excited frequency. In the presence of an external magnetic field containing a component aligned appropriately for the type of core, the saturation cycle reaches an altered state. During the altered saturation cycles, a current is induced on the pick-up coil, which is read through the circuit and used to measure the strength of the background magnetic field. Based on these interactions, *Primdahl [1979]* shows that the basic fluxgate equation is:

$$V = nAB_{ex}(1 - D)(d\mu_r/dt) / [1 + D(\mu_r - 1)]^2 \quad (2.5)$$

where V is the induced voltage, n is the number of turns of the coil, A is the average cross-sectional area, B_{ex} is the external magnetic field component parallel to the core, μ_r is the relative permeability of the core, and D is a demagnetization factor. The demagnetizing factor depends on the materials and style of core used. Thus, by recording the induced voltage and knowing the other properties of the magnetometer, the external magnetic field can be found.

2.2.2 Derivation of AE Index

Davis and Sugiura [1966] defined the auroral electrojet indices as a measure of the strength of the auroral electrojet, Section 1.2.3. Auroral indices are also often used to characterize substorm activity in the auroral zone. The indices are derived from the horizontal component of the magnetic field observed at magnetometer stations within a network around the northern auroral zone. Table 2.1 shows the list of stations used in the derivation of this family of indices. The magnetometer stations at Barrow and College are in the same region as PFISR (Figure 2.2). During winter 2007, a new magnetometer station was put online in Sanikiluaq, Canada to replace the station closing in Poste-de-la-Baleine, Canada.

To ensure that the data are reliable, readings from the observatories are normalized

Table 2.1: Magnetometer stations used in AE derivation.

| Station | Geographic | | Geomagnetic | | Station Notes |
|---------------------|------------|-----------|-------------|-----------|-----------------|
| | Lat. (°N) | Lon. (°E) | Lat. (°N) | Lon. (°E) | |
| Abisko | 68.36 | 18.82 | 66.60 | 114.66 | |
| Dixon Island | 73.55 | 80.57 | 64.04 | 162.53 | |
| Cape Chelyuskin | 77.72 | 104.28 | 67.48 | 177.82 | |
| Tixie Bay | 71.58 | 129.00 | 61.76 | 193.71 | |
| Pebek | 70.09 | 170.93 | 63.82 | 223.31 | |
| Barrow | 71.30 | 203.25 | 69.57 | 246.18 | |
| College | 64.87 | 212.17 | 65.38 | 261.18 | |
| Yellowknife | 62.40 | 245.60 | 68.87 | 299.53 | |
| Fort Churchill | 58.80 | 265.90 | 67.98 | 328.36 | |
| Narssarssuaq | 61.20 | 314.16 | 69.96 | 37.95 | |
| Leirvogur | 64.18 | 338.30 | 69.32 | 71.04 | |
| Sanikiluaq | 56.5 | 280.8 | 66.6 | 349.7 | Open: 12/2007 |
| Poste-de-la-Baleine | 55.27 | 282.22 | 65.45 | 351.77 | Closed: 11/2007 |

prior to the final data release. For each station and each month, the magnetometer data is normalized by taking the average of all the data from that station on the five international quietest days to create a base value which is then subtracted from each of the 1-min interval data values at that station in that month. The superposition of the normalized data from each station is then used to determine the various auroral indices.

Figure 2.3 illustrates derivation of the four auroral electrojet indices that comprise the electrojet index series. It shows an example of magnetometer measurements on May 15, 2007, a representative event for the dataset considered in this thesis. All individual magnetometer readings (from 12 stations in Table 2.1) are omitted here to keep the diagram readable, but all of them were between the green and blue lines that form the upper and bottom envelope, respectively, of the 12 horizontal components of magnetic field perturbations. (The red line is not the upper envelope but a separately derived

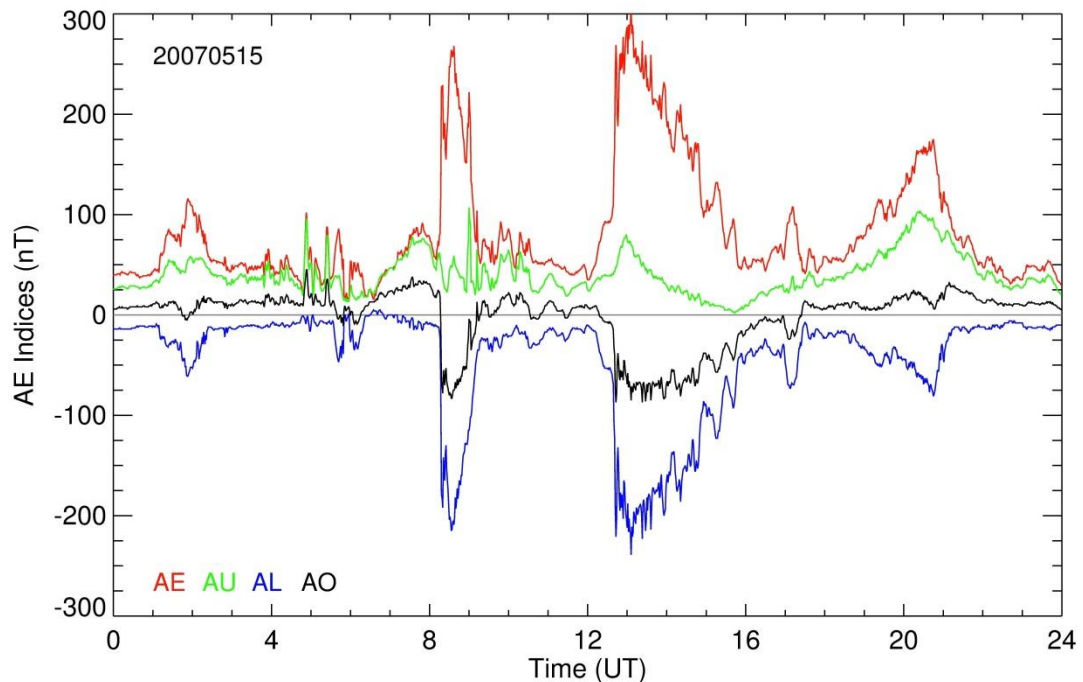


Figure 2.3: Auroral electrojet index measurements for May 15, 2007. Upper envelope (green) and lower envelope (blue) values are taken from the highest and lowest readings, respectively, across the magnetometer network. AO (black) is derived from the average of AL and AU. AE (red) is the difference between the upper and lower index values.

positive AE index described below). The time resolution is 1 min.

The auroral upper index (AU) is the most positive value within the network at the time of determination and is considered to be a measure of the eastward electrojet strength (green line in Figure 2.3). The lower index (AL) is the most negative value in the network and is a measure of the westward electrojet (blue line). The combination of these two index values creates the other two values as follows. The AO index (black line) is defined as the mean between the upper and lower indices:

$$AO = (AL + AU)/2. \quad (2.6)$$

The AO index is considered to be an approximation for the equivalent zonal current strength. Finally, the AE index (red line) is defined as the difference between the upper and lower envelopes:

$$AE = AU - AL. \quad (2.7)$$

The value obtained from the calculation for AE is considered to be a representation of the overall auroral electrojet strength and is commonly used as an indicator of auroral activity, particularly in the absence of other reliable auroral indicators such as global auroral observations (e.g. EUV/FUV satellite measurements). Moreover, AE measurements are nearly continuous and not affected by cloud coverage or propagation conditions. Further, the AE indices are not computationally intensive to use and their routine time resolution of 1 min makes it possible to match them with measurements taken at other resolutions by employing post-integration. Finally, sorting the data in AE bins has become a standard practice in space physics research, particularly in studies with some Space Weather applications, e.g. those that attempt to predict occurrence and/or strength of certain events [e.g., *Werner and Prölss, 1997; O'Brien et al., 2002; McWilliams et al., 2008; Golden et al., 2012*].

In the current thesis, the dynamics of the nighttime E-region are investigated and AE index readings are used as a proxy for auroral activity. All AE data employed here were obtained from the World Data Center for Geomagnetism, Kyoto at 1-min resolution. They were further post-integrated using the same ~15-min intervals as for the PFISR

electron density data. More details on the data analysis are given in the following two sections that describe the original research results of this thesis.

3. Dynamics of Nighttime E-Region Electron Content

This section describes results from the first original research project which focused on the behavior of nighttime E-region electron content. The aim of this project is to improve our understanding of the influence of geomagnetic conditions on the dynamics of the E-region during solar cycle minimum. A description of the data processing for this project is presented in Section 3.1. This is followed by analyses of the E-region electron content and AE index in terms of their diurnal and seasonal variations, Section 3.2, and in terms of solar zenith angle effects, Section 3.3. Analysis of E-region contribution to the total electron content is then presented in Section 3.4.

3.1 Determination of Electron Content and Corresponding AE Index

PFISR observations of electron density generally utilize two data sets: alternating code (AC) and long pulse (LP), as described in Section 2.1.3. To illustrate the method employed in this thesis for deriving the E-region electron content estimates from the electron density data and corresponding mean AE index values, Figure 3.1a shows an example of these datasets at their “raw” or native resolutions and results of the data reduction procedure employed.

Figure 3.1a shows the PFISR electron density on May 1, 2007, with AC data up to 250 km and LP data above 250 km. Determination of the electron content of the E-region relies on observations made using AC mode, where the upper limit of the E-region is set to be at 150 km in altitude, as displayed in Figure 3.1a by the horizontal red line.

The electron content of the E-region is calculated by integrating PFISR electron density from the lowest AC observations of ~82 km up to the top of the E-region of ~150 km. The integrated total electron content in the E-region that is obtained from PFISR electron densities up to an altitude of 150 km is denoted throughout this thesis as $ITEC_{150}$ in order to be consistent with other studies that also used ISR-inferred ITEC [e.g. *Lilensten and Cander, 2003; Makarevich and Nicolls, 2013*]. Total electron content units (TECU) are used to describe the integrated electron content values in this thesis where $1 \text{ TECU} = 10^{16} \text{ electrons per m}^2$.

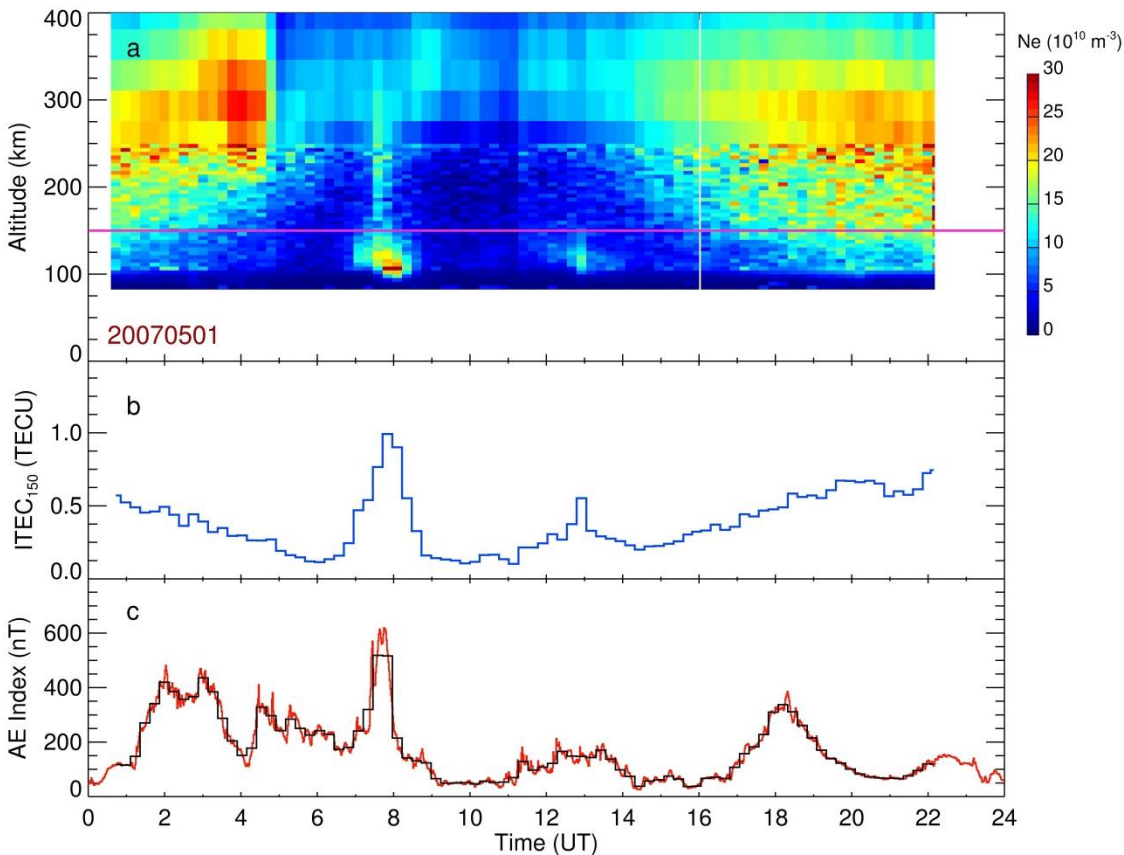


Figure 3.1: Electron density, electron content, and AE variations on May 1, 2007. (a) PFISR electron density at various altitudes in 15-min intervals. Densities obtained with the alternating code are displayed up to 250 km with long pulse values shown above 250 km. E-region ceiling is set at 150 km, represented by the pink line. (b) E-region electron content (up to 150 km) for each PFISR time interval. (c) AE index for 15-min averaged (1-min standard) intervals represented by black (red) line.

Figure 3.1b shows the derived ITEC₁₅₀ values from the densities shown in Figure 3.1a above. ITEC₁₅₀ displays a gradual decrease as time approaches local midnight (~11 UT) and a gradual increase as time approaches midday (23 UT), showing the effects of diurnal variation. Importantly though, superposed on this diurnal pattern there are two nighttime disturbances, with electron density in the E-region enhanced near 08 UT and to a lesser degree near 13 UT. Correspondingly, ITEC₁₅₀ displays a large increase around 08 UT and a smaller increase near 13 UT.

The AE index “raw” data provided by the World Data Center (WDC) in Kyoto is at 1-min resolution. This data for May 1, 2007 is displayed in Figure 3.1c by the red line.

However, the analyzed data from PFISR is provided in 15-min intervals. Thus, to get a representative value for AE index for each PFISR data point, the values obtained from the WDC are averaged in timespans corresponding to the intervals of PFISR observation, as indicated by the black histogram in Figure 3.1c. Since there were no PFISR IPY observations at 22–24 UT, only “raw” AE measurements (red line) are shown there.

Comparing the datasets represented by the blue and black lines in Figures 3.1b and c, respectively, one can see that, while the diurnal pattern of $ITEC_{150}$ is not reflected in AE variation, both disturbances in $ITEC_{150}$ (near 07 and 13 UT) have associated disturbances in AE. Moreover, even their shapes match well (sharp peak at 07 UT and more extended and weaker maximum at 13 UT). On the other hand, there were other AE disturbances that did not have any corresponding signatures in $ITEC_{150}$ (at 01–08 UT and near 18 UT). These auroral disturbances that did not have associated signatures in $ITEC_{150}$ were observed away from the midnight sector and since this thesis is concerned with nighttime disturbances, the following analysis is restricted to the 04–18 UT period. In doing this at least a significant subset of all non-matched AE- $ITEC_{150}$ disturbances is excluded. One reason why these non-matched disturbances are observed is that AE is a global index and it does include magnetic signatures of disturbances that occurred on the opposite side of the auroral oval relative to the location of interest (PFISR in this case). By restricting the period of observation to 04–18 UT, the contribution of these events is significantly reduced. Further, in the following analysis the data is sorted in UT and solar zenith angle, which provided an opportunity to examine and further reduce contribution of these non-local disturbances.

A systematic comparison between all matched values of $ITEC_{150}$ and AE between 04–18 UT is presented below. Figure 3.2 represents an entire month of data of May 2007. Figure 3.2a shows the minimum, maximum, and mean values of $ITEC_{150}$ during nighttime, where the mean is represented by the red bar and the range of minimum to maximum values is represented by the grey bar. Days with less than 4 data points during nighttime are not considered and not shown in Figure 3.2a. Similarly, Figure 3.2b shows the minimum, maximum, and mean values for the raw AE index during nighttime.

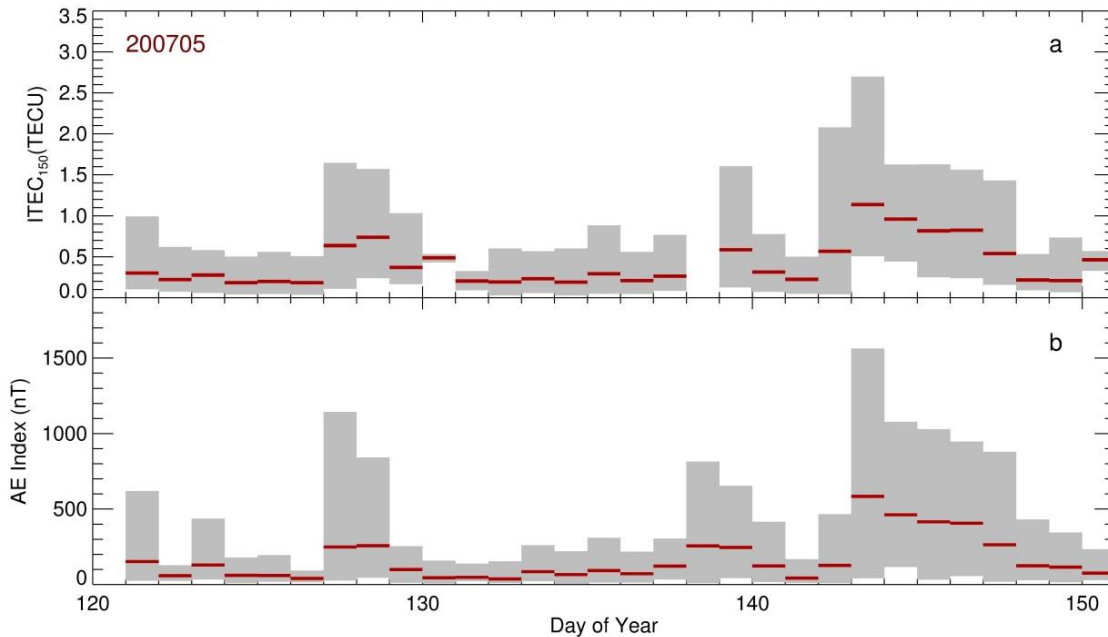


Figure 3.2: Nighttime electron content and AE index in May 2007. Minimum, maximum, and mean (a) E-region electron content and (b) AE index during nighttime (4–18 UT) for each day in May 2007. Minimum and maximum range is represented by the grey bar, while the mean is represented by the red bar.

When comparing each day of May between the two panels, it is apparent that there is a general tendency for days of greater mean $ITEC_{150}$ to have a greater mean AE index. Likewise, on nights of smaller mean $ITEC_{150}$, the mean AE is also reduced. This is consistent with a similar association seen in Figure 3.1 for one day only. To get a more complete picture of this behavior, all available data for nighttime during the year 2007 is plotted in Figure 3.3. As in Figure 3.2, the minimum, maximum, and mean values of $ITEC_{150}$ and AE index are displayed in panels (a) and (b), respectively. The month of May that was presented in Figure 3.2 is highlighted in yellow. For the nights with sufficient data points, the same trend of increased (decreased) mean $ITEC_{150}$ occurring during nights of increased (decreased) mean AE index is apparent throughout the entire year. The other feature in Figures 3.2 and 3.3 is that variations in maximum, minimum, and mean values look very similar. That is, when one is rising (falling) this is usually accompanied by a rise (fall) in the two other values. This allows for focus on the analysis of the average values only.

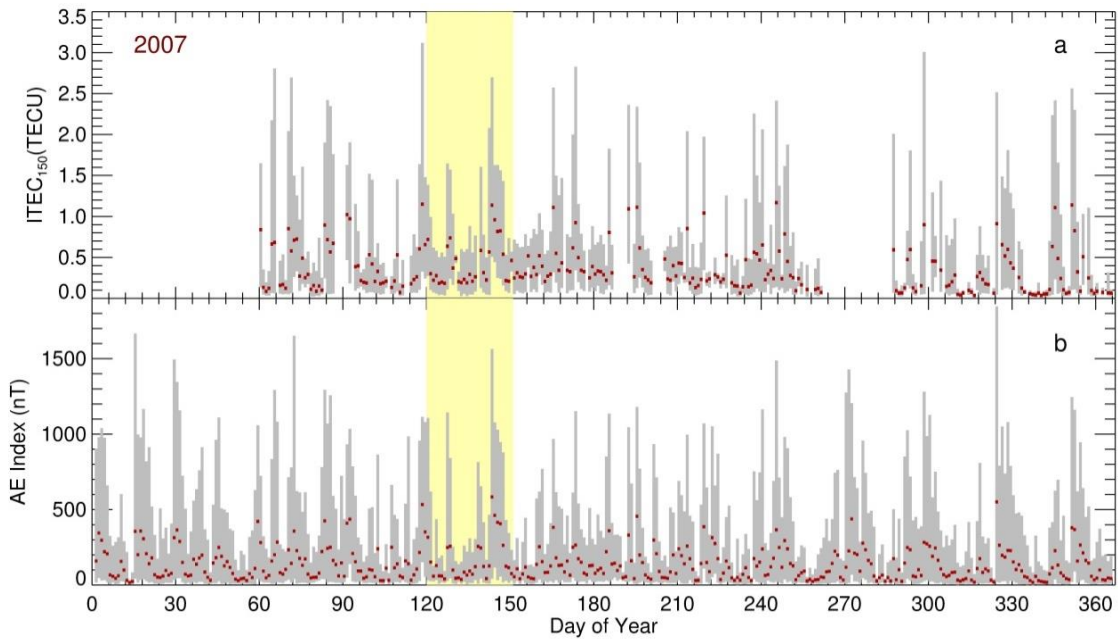


Figure 3.3: Nighttime electron content and AE index in year 2007. As in Figure 3.2, but for the entire year 2007 with available PFISR IPY data. May 2007 highlighted in yellow.

While Figures 3.2 and 3.3 show the possibility of significant positive correlation between nightly averages of $ITEC_{150}$ and AE index, it is useful to reorganize the data in a different manner. Splitting up the data by month, the averages of $ITEC_{150}$ and corresponding AE index are taken for each hour in that month to examine the behavior versus both time of the day and season. Figure 3.4 displays the hourly averages for each month in 2007 for (a) $ITEC_{150}$ and (b) corresponding AE index. Present in both panels of Figure 3.4 are black lines, which represent the separation of data for seasonal analyses. Spring is defined as February through April, summer is May through July, autumn is August through October, and winter is November through January.

In Figure 3.4a, E-region electron content, $ITEC_{150}$, is the greatest surrounding the middle of the night (~ 11 UT) during the autumn and spring, as well as between approximately 04–07 UT and 15–18 UT during summer months. The increased $ITEC_{150}$ during summer is primarily due to diurnal variation from the increased length of day at the PFISR latitude. The late-night increases during the remainder of the year are due to

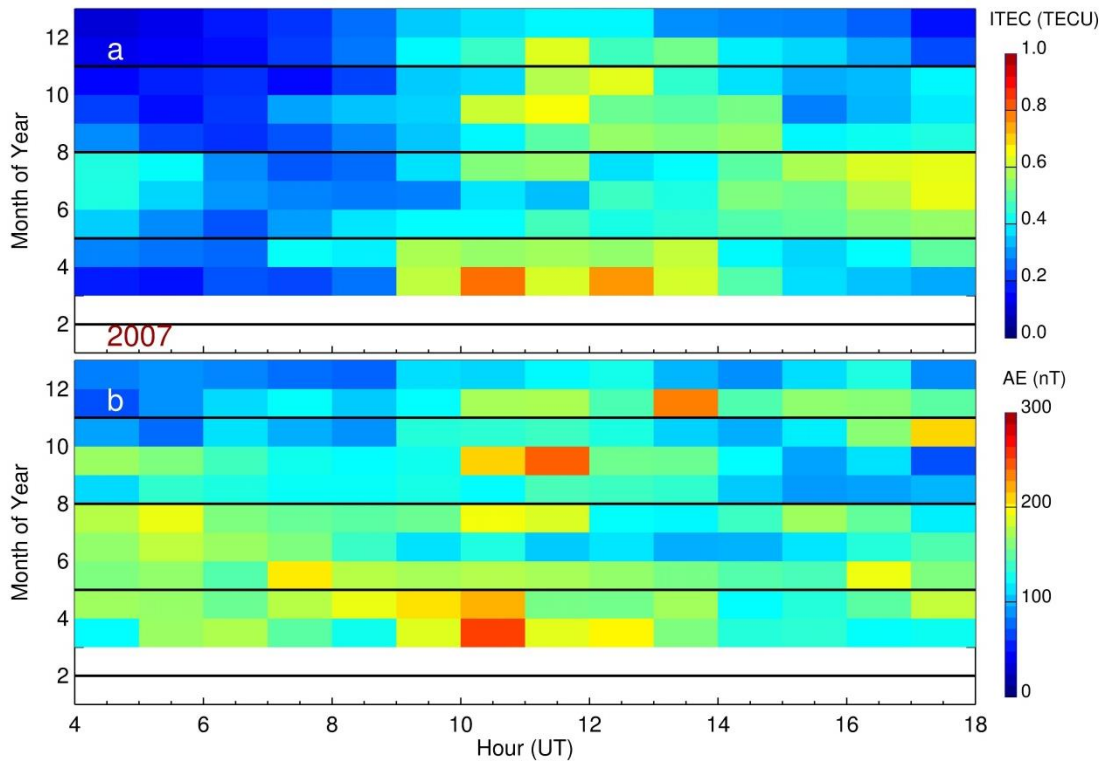


Figure 3.4: Average E-region electron content and AE index. Shown are (a) E-region electron content $ITEC_{150}$ and (b) AE index averaged over each hour for each month in 2007. Black lines indicate months used in seasonal analyses. The color bars for $ITEC_{150}$ and AE are given to the right of the respective panel.

the other effect; this particular phenomenon is what is investigated and discussed in more detail in this project.

Figure 3.4b shows the AE index also averaged for each hour and for each month using only the values which had corresponding PFISR information. Concentrating on the timespan roughly surrounding local midnight (08–14 UT) for the year, there is some evidence of a positive correlation between AE and $ITEC_{150}$. For the most part, where AE index is markedly greater, the $ITEC_{150}$ for that month and time is greater than those in the nearby hours. Outside of the near-midnight period, there appears to be less of a relationship between the two datasets. That is, there are more times of low $ITEC_{150}$ that align with higher AE index and high $ITEC_{150}$ with lower AE index than in the near-midnight period. The color-coded presentations like Figure 3.4 do not necessarily reflect well a true extent of a correlation. Using a proper correlation analysis for the two datasets

in Figure 3.4, a value of 0.86 (0.81) is obtained for the linear (rank) correlation coefficient. This is well above a 99.9% confidence value of 0.22 for this dataset, which means that the correlation between hourly E-region electron content and AE index is statistically significant. Nevertheless, with the above-noticed difference between the midnight and other sectors in mind, it becomes of particular interest to investigate the relationship between $ITEC_{150}$ and AE index with respect to the time of night.

3.2 ITEC-AE Relationship: Diurnal and Seasonal Variations

In the previous section, AE and $ITEC_{150}$ displayed a positive correlation and some evidence of a relationship to the time of day. To investigate how the two quantities behave during different times, first the data were broken down into monthly sets. The $ITEC_{150}$ and corresponding AE index during nighttime were then plotted against each other for each month. The difference with the previous analyses displayed in Figures 3.2–3.4 is that no averaging of any kind was performed here (apart from that required to match PFISR and AE measurements for each of the 15-min intervals). The correlation and linear fit analyses were then performed on the data for that month.

The entire dataset for the month of May 2007 is plotted in Figure 3.5, with data points color coded in the hour of the day. The color bar is given to the right of the diagram. All available data points were used in the linear fit and correlation calculations (1,484 points for this month). The correlation of $ITEC_{150}$ and AE index for the month of May is moderate at best, with a coefficient of 0.496. As demonstrated later in this section, monthly correlation coefficients are greatest during winter months and smallest for summer months, so the given example of May 2007 is in between these two cases.

A large number of data points in Figure 3.5 are grouped below 0.5 TECU and 200 AE, where the largest electron content observations are made during the earliest (blue points) and latest (red points) allowed times in the dataset. For these data points, the increased electron content is due primarily to diurnal variation from periods near sunrise and sunset. Outside the lower corner of the plot, there is a wider spread between data points. A quick inspection shows that points corresponding to times near midnight

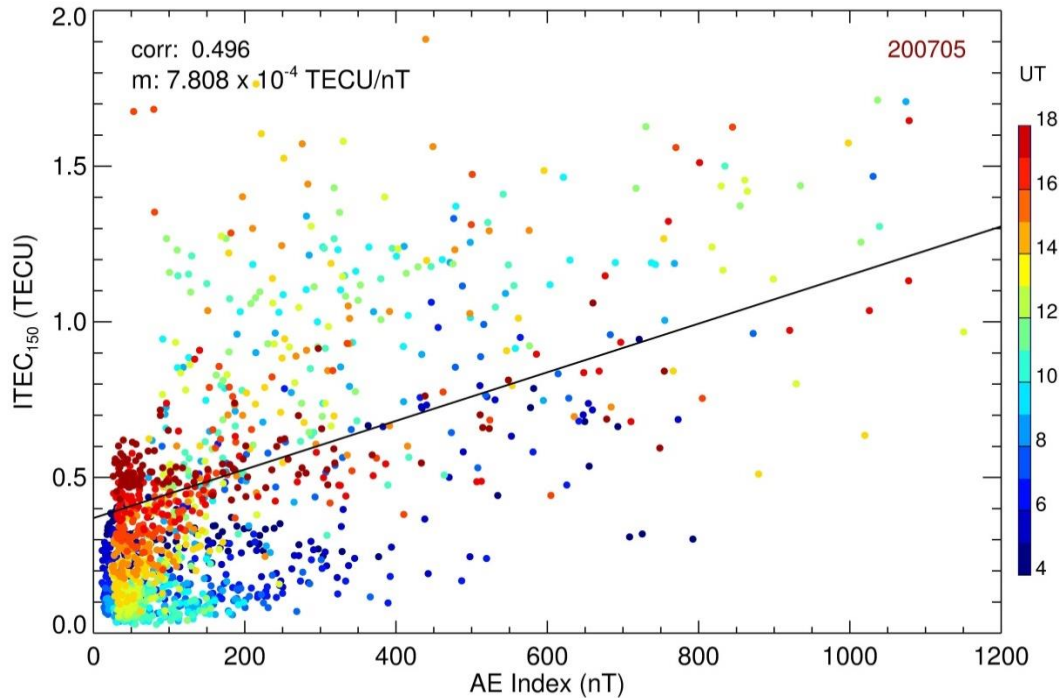


Figure 3.5: E-region electron content versus AE index for May 2007. The points are color-coded in hour of day. 1,484 total data points are included in the correlation and linear fit. The linear Pearson correlation and slope of the linear fit for the entire month are displayed in the figure.

(lighter blues through yellows) mostly occur above the linear fit line while evening and morning times (dark blues and reds) mostly occur below the linear fit line in this region.

The apparent difference in behavior between each hour in Figure 3.5 prompts us to break down each monthly dataset into separate hourly subsets of data. In Figure 3.6, each panel contains the observations from a different UT hour for May 2007. For each panel, the Pearson correlation coefficient and linear slope are calculated and shown in the top-left corner. The color scheme for data points matches that in Figure 3.5.

In the month of May, the correlation between $ITEC_{150}$ and AE for separate hourly blocks is greater than the correlation of the entire month. Correlation values are greatest near midnight (07–12 UT) with the exception of an increased correlation around 16 UT. The same analysis was conducted for every other monthly dataset. The results of this analysis were very similar to those from another analysis presented later in this section, and for this reason not presented here. In general, both analyses showed that the

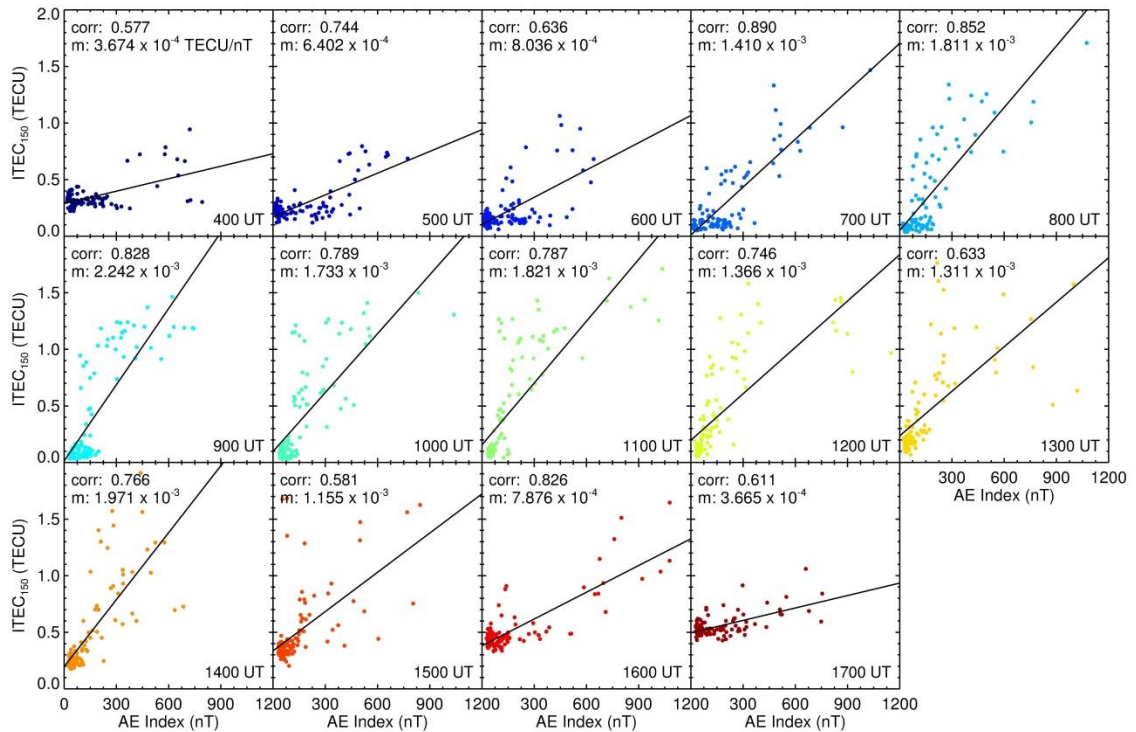


Figure 3.6: E-region electron content versus AE index for each hour. The same as Figure 3.5, but with the data separated according to the UT hour.

correlation coefficients have a greater tendency toward higher values near midnight. Similarly, the slope of the best-fit line for each hour of data is highest nearer to midnight and lowest around dawn and dusk hours.

In addition to separation of the data in the monthly and hourly subsets, as illustrated in Figure 3.6, the dataset was also sorted according to the season and hourly sector, and the same correlation and best fit analyses conducted. Seasons were defined as follows: spring from February through April, summer from May through July, autumn from August through October, and winter from November through January. As PFISR operations started in March 2007, this means that spring and winter of 2007 contained two months of data while summer and autumn contained three. Despite this difference, there was a reasonably large dataset for each season so that a meaningful analysis could be conducted for each season.

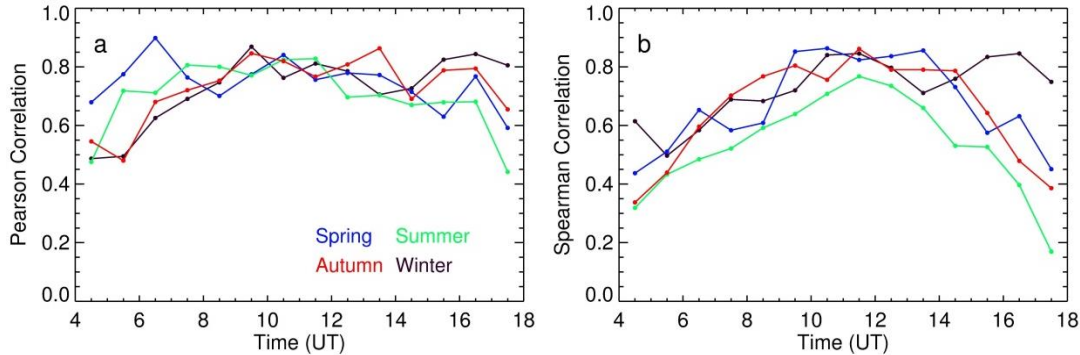


Figure 3.7: Correlation between E-region electron content and AE index versus UT. (a) Pearson and (b) Spearman correlations between E-region electron content and AE index for different hourly intervals and different seasons in 2007. The 99.9% confidence level values were all above 0.25.

The results of correlation analysis are presented in Figure 3.7, with the (a) Pearson and (b) Spearman correlation coefficients shown separately. The Pearson correlation is a measure of how linear a relationship is, while the Spearman correlation is a measure of how well a relationship can be described by a monotonic function. The 99.9% confidence values were all larger than 0.25 and hence correlations were highly significant.

The Pearson correlation values show a trend for greatest correlation to be near magnetic midnight (11 UT) for all seasons, with the exception of spring that has the main maximum at 06 UT. Nevertheless, the spring season has a secondary peak at 11 UT which is only marginally smaller. The most similar correlations between seasons occur at 09–12 UT. On either side of this time, correlation values differ between seasons.

The Spearman correlation coefficients display a more dramatic difference in values but more consistent behavior between different seasons. In particular, there is a much better defined peak in the correlations of each season using the Spearman method, centered around 11 UT, e.g. compare green curves for panels (a) and (b). This suggests that, if the $ITEC_{150}$ and AE are related, this relationship is more likely to be non-linear. The other important feature in Figure 3.7 is that $ITEC_{150}$ and AE index have the best correlations near midnight using either correlation method. The interpretation for this feature is offered in Section 3.5.

3.3 ITEC-AE Relationship: Solar Zenith Angle Effects

The diurnal and seasonal effects are related to a large extent since both are due to variation in the Sun's position with respect to a location in question. Thus, rather than focusing on hourly time blocks, it is useful to look at the solar zenith angle (SZA) χ when considering solar effects on the E-region dynamics. The same basic structure for analysis as outlined in Section 3.2 can be applied to SZA χ .

Figure 3.8 is the same plot of one month (May 2007) of $ITEC_{150}$ and AE index data as Figure 3.4, except that here all data points are color coded in SZA χ in 10° increments. The color bar is given to the right. As in Figure 3.4, many points in Figure 3.8 tend to cluster in the left-bottom corner below 0.5 TECU and 200 nT. In this presentation, however, a clear color-coding pattern is evident in this corner; low SZA χ (blue and green) cluster at the top, while high SZA χ (orange and red) make up the lower portion. This is a clear indication that these points mostly represent quiet times, undisturbed by the auroral activity, and the electron content variation is mostly due to SZA effects:

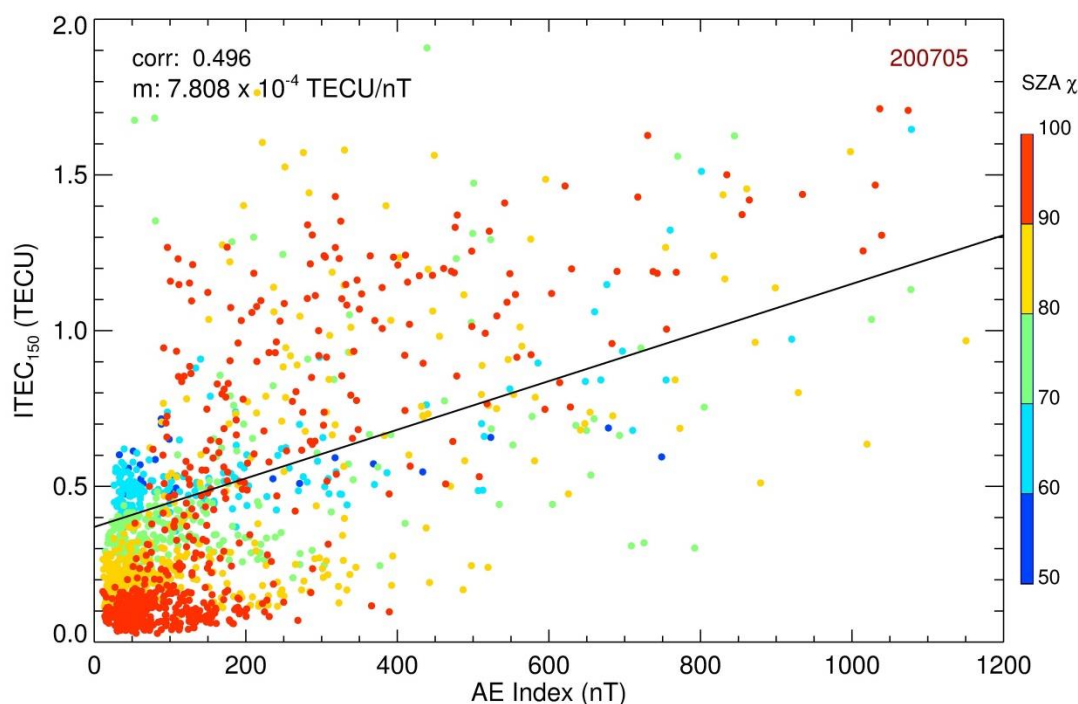


Figure 3.8: E-region electron content versus AE index for May 2007, color-coded in SZA χ in 10° increments.

higher for lower SZA or higher solar elevation. Outside this corner, data points with higher SZA values (red-orange) tend to appear above the line of best fit while data points corresponding to lower SZA values (blue) tend to appear below. These points are primarily due to auroral activity.

Following the same method as that described in Section 3.2, the month of data is broken down into subsets based on 10° increments of SZA χ . Each panel in Figure 3.9 corresponds to a 10° increment of SZA χ in ascending order, color coded in the same manner as Figure 3.8. For each panel, the Pearson correlation and linear fit coefficients are also shown. In general, larger SZA χ tends to have a larger correlation, with the exception of the 60° – 70° subset, which for this particular month is greater than the preceding and following SZA χ segment. The slope of the linear fit consistently increases as the angle of SZA χ increases such that the greatest slope occurs for SZA $\chi = 90^\circ$ – 100° .

As in Section 3.2, the data points were reorganized into seasonal sets and further

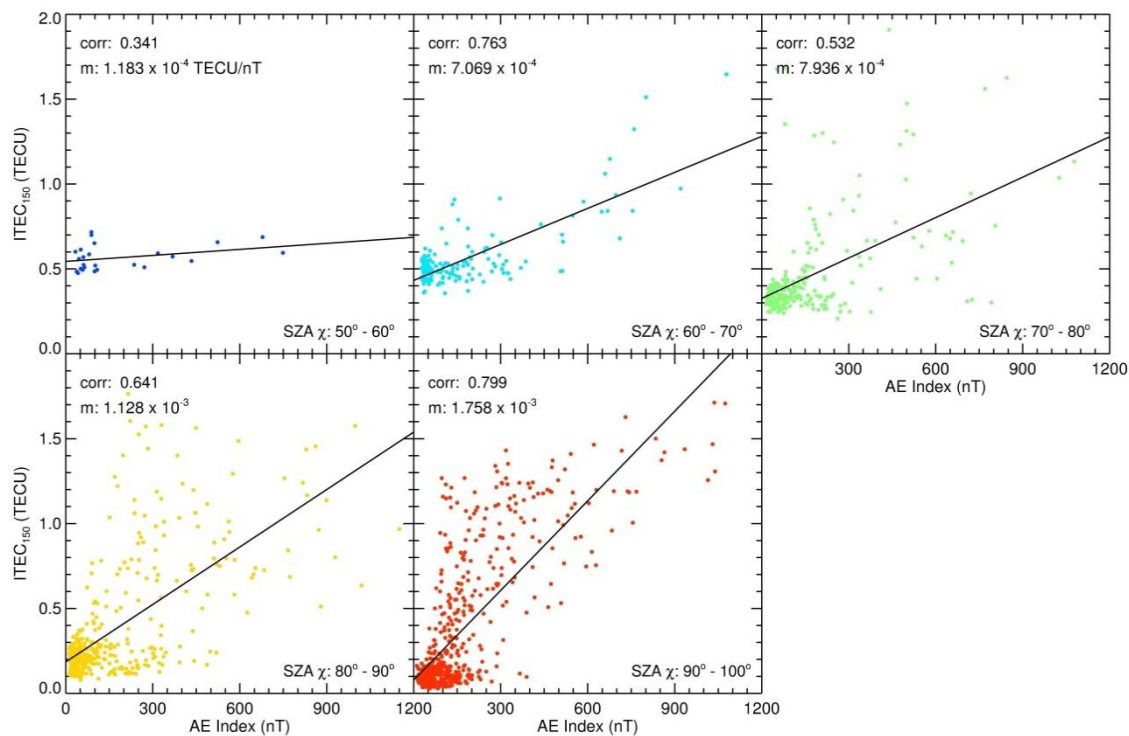


Figure 3.9: E-region electron content versus AE index sorted in SZA. The same as Figure 3.8, but for subsets separated in 10° SZA increments.

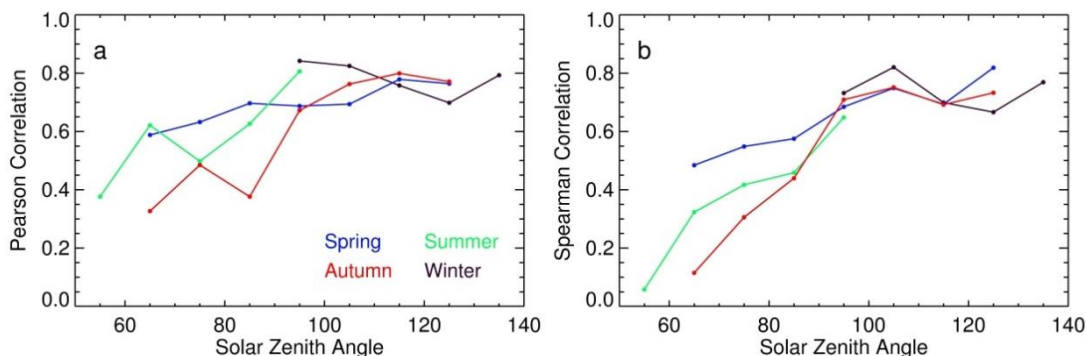


Figure 3.10: Correlation between E-region electron content and AE index versus SZA.

correlations were calculated for each 10° SZA χ increment in each season. Figure 3.10 shows the (a) linear Pearson and (b) rank Spearman correlation coefficients versus SZA χ .

Linear correlations generally increase with SZA χ up until near 100° . After an angle of 100° , the correlation between $ITEC_{150}$ and AE index appears to level off. Rank correlations show the same trend, but much more clearly. That is, correlation coefficients increase with SZA χ , reaching a maximum near 100° and leveling off above 100° . The differences between different seasons are most pronounced at lower SZA values. At these values, the highest correlations are observed during the spring season.

3.4 E-region Contribution to the Total Electron Content

During quiet nighttime, the electron content of the E-region reaches its smallest value, as does the total electron content of the ionosphere. However, during times of activity, $ITEC_{150}$, and by extension TEC, increases. One aspect of the ionosphere that has not been well researched is the extent of nighttime E-region contribution to TEC (or percent contribution of $ITEC_{150}$ to TEC) under various geomagnetic conditions. An estimate for the TEC can be inferred from PFISR electron density observations by applying a similar integration in altitude only for all available data. Even though PFISR data in the field-aligned beam (beam 64157 in the PFISR numbering scheme) only extends up to 663 km in altitude (while the term TEC is normally reserved to GPS measurements that cover the altitude range 0 to 20,200 km) the ISR- and GPS-inferred

TEC estimates exhibit correlations of ~ 0.9 and ratios of ~ 0.75 [Makarevich and Nicolls, 2013]. Therefore, in this section PFISR estimates of TEC or ITEC_{663} or simply ITEC are used as a proxy for TEC and compared with ITEC_{150} . One has to remember though that in order to estimate a “true” $\text{ITEC}_{150}/\text{TEC}$ ratio one has to apply the following correction: $\text{ITEC} = 0.75 \text{ TEC}$ and $\text{ITEC}_{150}/\text{TEC} = 0.75 \text{ ITEC}_{150}/\text{ITEC}$.

The ITEC values were calculated from the lower through upper bounds of PFISR observation altitudes: approximately 82–663 km. In order to obtain ITEC, AC data were integrated between 82–250 km and subsequently added to the integrated LP data between 250–663 km. ITEC_{150} was determined as described in Section 3.1. Furthermore, to eliminate times where there was insufficient data for proper comparison between ITEC and ITEC_{150} , it was required that at least 70% of the AC data was available for ITEC_{150} calculations and at least 70% of the altitude gates for the combined AC/LP dataset was available for the calculation of ITEC.

Percent contribution of E-region electron content to nighttime TEC for May 2007 is displayed versus time in Figure 3.11 with data points color-coded in the AE index for that 15-min time interval. For most data points with low AE index (dark blue), the contribution of ITEC_{150} to TEC does not exceed 10%. These points cluster at the bottom of the cloud of points in Figure 3.11 forming a lower envelope of all data points or lower limit that changes systematically with UT. This feature is a manifestation of diurnal behavior, where the lowest percentage occurs during the middle of the night and highest percentage during dusk and dawn, when this lower envelope is considered.

Time intervals which had a percent contribution significantly above this diurnal variation envelope appear mostly in lighter blue (moderate AE) through red (high AE) in Figure 3.11. The greatest contributions came between approximately 08–14 UT, trailing off toward dawn and dusk. However, even throughout dawn (14–18 UT) and dusk (04–08 UT) the percent contribution is greatest from points with higher AE (>300 nT). The time intervals corresponding to the greatest percent contributions occur primarily during times with the greatest AE index, indicating that ITEC_{150} during active periods increases to a greater degree than the electron content of the entire ionosphere.

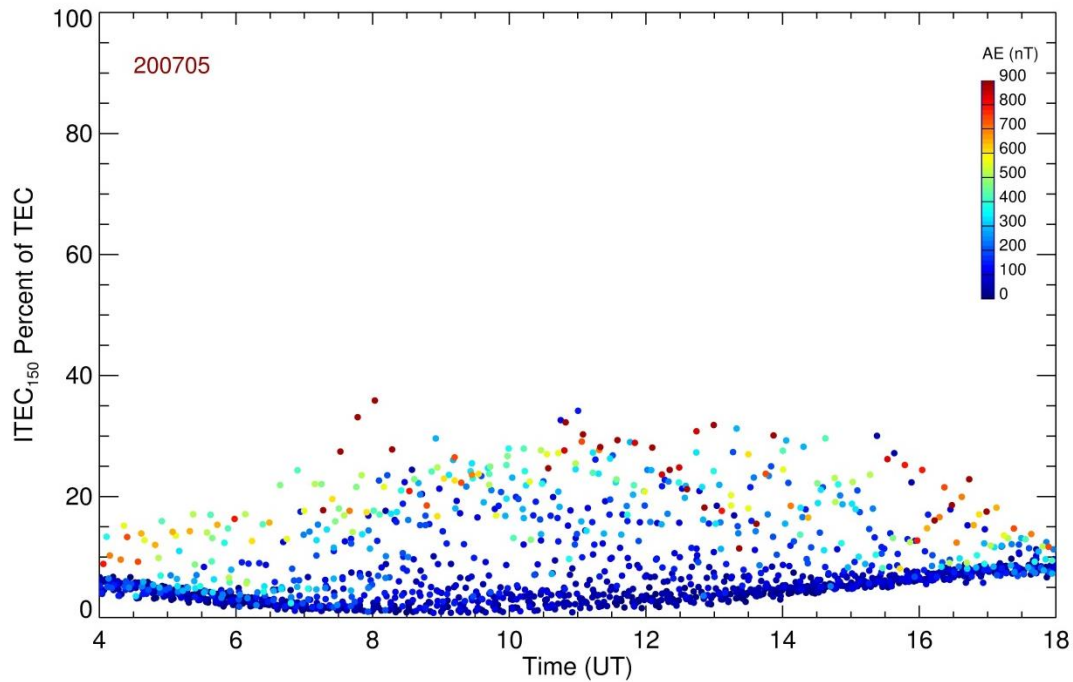


Figure 3.11: E-region contribution to TEC in May 2007. Percent contribution of the E-region electron content to PFISR-inferred total electron content (TEC) for May 2007. The points are color-coded in AE index, as given by the color bar in the top-right corner of the diagram.

Applying the same methods to all available PFISR data (March 2007–December 2010) and sorting by seasons, as defined previously, results in Figure 3.12. Each column of the figure represents a different year while each row represents a different season. The reduced number of data points in spring 2009 as compared to the other years is due to a combination of increased usage of PFISR for non-IPY-compatible experiments and the minimum data requirements for the calculation of $ITEC_{150}$ and TEC not being met.

The percent contribution during the summer for all years is comparable to that in May 2007 described previously. Winter contribution of $ITEC_{150}$ to TEC does not show a decrease in the dusk and dawn sectors and appears to take a wide range between 5%–60% for any time and for any AE index. While there is still a tendency for more active time intervals to have a greater contribution, data points from quiet intervals have a greater range of percent contribution which overlaps the range of contribution during active intervals. Thus the lower envelope cluster is less evident. Unlike summer, there is

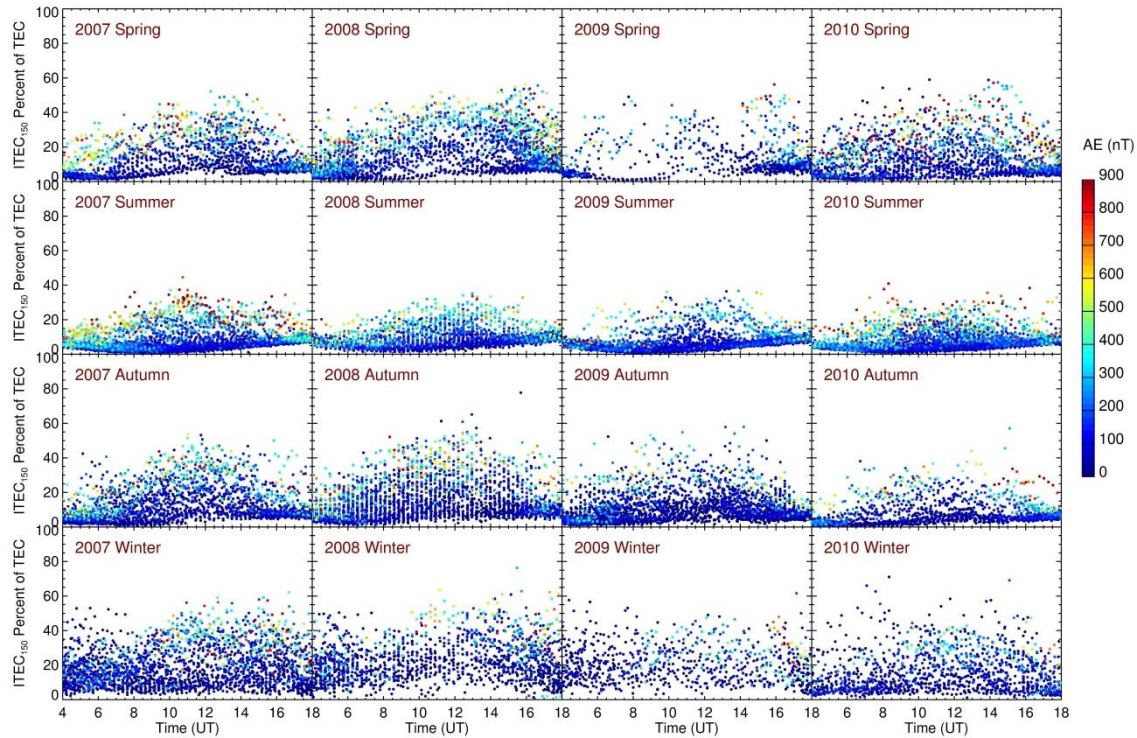


Figure 3.12: E-region contribution to TEC in 2007–2010. As in Figure 3.11, but for all 4 seasons and for all years 2007–2010. Spring is February – April, summer is May – July, autumn is August – October, and winter is November – January.

less distinction between active and quiet periods and no particular time interval shows a tendency for higher contribution. This is likely due to the fact that both TEC and $ITEC_{150}$ are at their minima during nighttime in winter so that small changes in electron density cause a large swing in their relationship.

Behavior during spring and autumn seasons are comparable. There is a clear lower envelope of percent contribution for time intervals where AE index is low, similar to that in summer but not as well defined. Intervals with moderate-to-high AE index remain along the upper edge of data points in each year for spring and autumn, demonstrating, again, that the E-region contributes more to TEC during active periods as compared to quiet times. Both spring and autumn show a general tendency to have the greatest percent contribution near the middle of the night.

Solar cycle influences are not easily discernible in the available data, except for in the autumn panels. The range of percent contribution of $ITEC_{150}$ to TEC increases

between autumn 2007 and autumn 2008, then decreases for the subsequent autumns. One notable thing about the autumn 2008 panel is the greater percent contribution range for intervals of low AE. While TEC and $ITEC_{150}$ should be nearer to their nighttime minima for quiet times, the percent contribution seems to be increasing. This implies that, at least for this particular season, $ITEC_{150}$ did not reduce as fast as TEC overnight.

3.5 Discussion and Summary

In this project, the dynamics of the E-region electron context were investigated using an extensive dataset collected by PFISR during the 4-year period under extreme solar minimum conditions. In particular, the relationship between $ITEC_{150}$ and corresponding AE values was analyzed using a number of different approaches. More specifically, the analyses in this section were performed with the goal of assessing factors that may control the E-region electron density, such as auroral disturbances and solar illumination, and studying the E-region contribution to TEC. From these analyses, the following main observations can be formulated.

The first notable result of the analysis performed in this section is a significant positive correlation between AE and $ITEC_{150}$ observed during nighttime. This correlation was observed in the minimum, maximum, and mean nightly values, Figures 3.2 and 3.3, where days with an increased (decreased) mean value of $ITEC_{150}$ corresponded to the days of increased (decreased) mean AE. This correlation was also observed in hourly averages for each month, Figure 3.4. Correlation of the hourly averages in Figure 3.4 was reflected in a significant linear (rank) correlation coefficient of 0.86 (0.81). The correlation between $ITEC_{150}$ and AE was also observed for datasets without any additional averaging (i.e. at 15-min resolution), Figures 3.5–3.10. When effects due to time of day, Figures 3.5–3.7, and SZA χ , Figures 3.8–3.10, were considered, the correlation between AE and $ITEC_{150}$ was varying in a systematic fashion (e.g. it was largest during the middle of the night), which strongly indicates that the correlative relationship between $ITEC_{150}$ and AE is real.

The explanation for the observed $ITEC_{150}$ –AE correlation may be offered as follows. $ITEC_{150}$ was derived from height-integrated electron density in the E-region. Free

electrons, and as such electron density, are caused by the ionization of particles, where the two forms of ionization in the ionosphere are photo- and impact-ionization, Section 1.2. The data in this study were restricted to the nighttime region where impact ionization is the primary mechanism. The AE index is a measure of the auroral electrojet strength, which can be used as an indicator of the overall auroral activity, Section 2.2.2. A correlation between $ITEC_{150}$ and AE thus suggests that $ITEC_{150}$ enhancements are associated with auroral particle precipitation.

There have been several previous studies that focused on factors that influence the auroral electrojets, each using different, but related, techniques and datasets [*Kamide and Vickrey, 1983; Davies and Lester, 1999; Kellerman et al., 2009*]. The basic outline of each study was to determine the electric field, conductivity, and current density in the ionosphere and then analyze the values to investigate how the auroral electrojet system was controlled by the electric field and conductivity. *Kamide and Vickrey [1983]* used ISR electron densities and a neutral atmosphere model to determine conductivities and LOS velocities to determine the electric field while using magnetometers to infer information about the electrojets. *Davies and Lester [1999]* used similar methods to determine conductivity and electric field while calculating current density from electric field and Hall and Pedersen conductivities. *Kellerman et al. [2009]* used cosmic noise absorption (CNA) as a proxy for conductance, ISR to determine electric field, and magnetometers to determine current. In each study, the results indicated that the electrojet in the magnetic midnight sector was dominated by electric conductance, while away from the midnight sector, the current variations were mostly due to the changing electric field.

Unlike the previously mentioned research, neither the electric field nor conductance were calculated in the analyses conducted in this thesis. Instead, the magnetometer-derived AE index was used as a proxy for electrojet current, as the measurements made by magnetometers primarily observe the Hall current, which is the main current in the electrojet system. While conductivity itself was not calculated, electron density is approximately proportional to conductivity; thus, $ITEC_{150}$ variations can be used as a rough approximation of the trends in conductivity. Therefore, the greater correlation

between $ITEC_{150}$ and AE seen near local midnight and high SZA χ is in support of the previous research, suggesting conductance as the dominant mechanism in the electrojet system near midnight. While this conclusion, by itself, is not necessarily new, it is now supported by the previously unexplored dataset. The other novel aspects of the current research include analyses of seasonal and solar zenith angle effects and potentially useful Space Weather implications, i.e. capability to predict enhancements in E-region electron content due to auroral particle precipitation based on simple AE values.

The other new aspect of this project was an estimate of the E-region contribution to TEC and an investigation into how this contribution changes for various conditions. This yielded an interesting result in that their ratio displayed diurnal variation in all seasons of the years considered, except for the winter. When plotting percent contribution against time of day, a lower envelope was seen, most notably during summer months, where the lowest contribution occurred in the middle of the night. Figure 3.11 showed this for the month of May 2007 while Figure 3.12 displayed this feature for all four years. This is not a trivial result since it concerns the $ITEC_{150}/TEC$ ratio rather than $ITEC_{150}$ or TEC themselves. Both $ITEC_{150}$ and TEC are expected to exhibit this diurnal behavior, but the behavior of the ratio is not necessarily expected to show any diurnal variation. The important result of this analysis thus is that it does. Thus, while TEC generally increases/decreases due to its diurnal variation, this behavior suggests that the rate of increase/decrease of $ITEC_{150}$ is greater so that it also increases/decreases their ratio.

Another result was that, in general, nighttime contribution of $ITEC_{150}$ increased during times of greatest AE index. This was visible in Figures 3.11 and 3.12 as the lighter blues through reds formed an upper bound in the plotted periods. For the nighttime $ITEC_{150}/TEC$ ratio to increase in this manner, precipitating particles must be in an energy range that suggests auroral origins, which provided another piece of evidence in support of the previously drawn conclusion linking enhancement in E-region electron density and auroral particle precipitation.

One final result to note regarding the $ITEC_{150}/TEC$ ratio is that during active periods, roughly 30% of PFISR-derived TEC was due to the E-region, Figures 3.11 and 3.12. In

other words, 30% of the electron content up to 663 km is due to lower altitudes between 82–150 km. This is a particularly important result since it is commonly assumed that the bulk of TEC is due to the F-region, normally the strongest and the most extended in altitude region of the ionosphere. While generally confirming this expectation, it was also demonstrated here that up to 1/3 is contributed by the lower E-region during active nights. Previous research by *Lilensten and Cander* [2003] compared electron content derived from EISCAT density measurements at 90–498 km, $ITEC_{498}$, to GPS-derived content, TEC. They estimated with their data that 50% of the content derived from GPS fell between the altitude range viewable by both EISCAT and GPS. Another study by *Makarevich and Nicolls* [2013] compared electron content derived from PFISR LP data, $ITEC_{663}$, to GPS-derived TEC. From their data they estimated that 25% of TEC fell between 660 km and the GPS satellite orbit and, by comparison to the results of *Lilensten and Cander* [2003], 25% fell between the maximum altitudes of EISCAT and PFISR (498 and 663 km). This means that in total PFISR roughly sees 75% of TEC seen by GPS. In comparison to these previous studies, $ITEC_{150}$ from this study used PFISR AC data rather than LP, for the same years as were considered in *Makarevich and Nicolls* [2013]. In addition, the roughly 30% contribution of $ITEC_{150}$ to PFISR TEC during active times then implies that the E-region contains roughly $0.3 \times 0.75 = 22.5\%$ of TEC during active nights, which is significant and has not been reported before.

4. Superposed Epoch Analysis of Nighttime E-Region Disturbances

Superposed epoch analysis (SEA) is a powerful statistical technique which is used to average data series surrounding a defined event type in order to reduce undesired data contribution (noise) and enhance the true response to a disturbance type. In the following analysis, the SEA technique is applied to electron density and geomagnetic data during selected periods of significant auroral activity. The aim is to improve our understanding of how the full electron density profile behaves versus time from the onset of auroral activity as well as the implied behavior of the particle precipitation spectra.

4.1 Disturbance Event Selection and Epoch Alignment

Events for analysis were chosen manually from criteria imposed on PFISR IPY data and AE data spanning from March 2007 through April 2011. Events were selected and event onset times were defined as described below. Events were restricted to nighttime hours between 04–18 UT where AC data was available from PFISR at least 30 min prior to and 120 min following onset. Events were further narrowed down based on the behavior of AE index values surrounding the event. In order to be included in the event list, AE must have exhibited a sharp rise over a small time span. More specifically, the minimum increase (rate) was set to 150 nT (20 nT/min). There were a total of 65 events found that fell within the specified requirements which were used in this analysis.

Figure 4.1 shows the distribution of the 65 selected events. With respect to the time of night, shown in Figure 4.1a, events are most concentrated near midnight with the peak number of events occurring at local midnight (~11 UT). There were no events included for analysis from the latest two nighttime hours considered and only one in either of the two earliest hours. In general, the further from midnight that the considered hour occurred, the fewer number of acceptable events were found in that hour. Figure 4.1b shows the distribution of selected events with respect to the month of the year. Selected events are most numerous in spring with the peak number of events occurring in March. Autumn has the second highest concentration of events. When applying SEA, the high concentration of events around a specific time of night as well as during a specific season result in a weighted contribution from seasonal and diurnal factors. To account for these

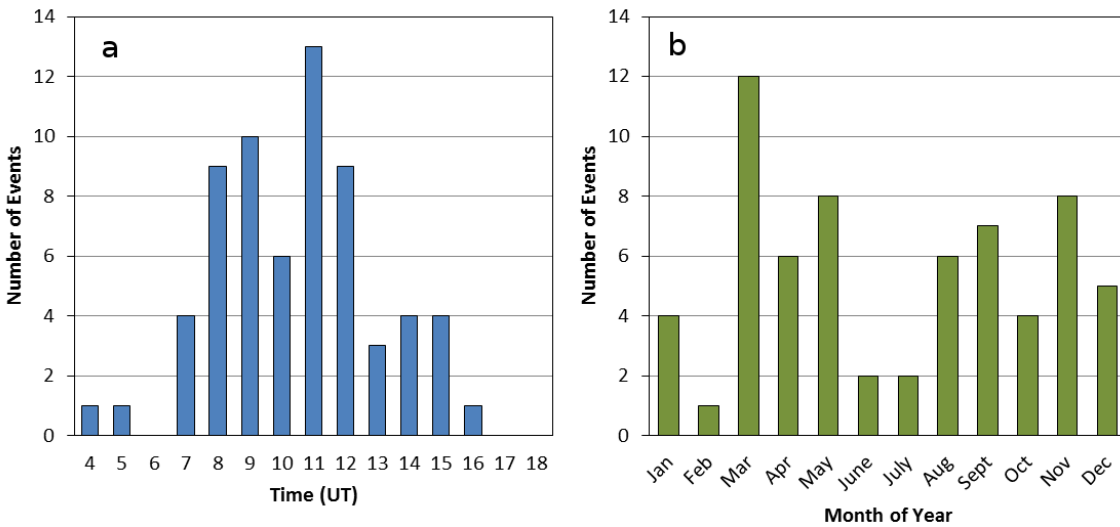


Figure 4.1: Distribution of selected events. Distribution of events shown for the (a) hour of the day and (b) month of the year.

weighted factors, the quiet-time contribution must be found (Section 4.2) and taken into consideration (Section 4.3).

Zero epoch for events was determined based on the time AE values started to rapidly increase. The AE index was used as a starting point for zero epoch selection because of the smaller increments between data points which yielded a clearer marker for onset as compared with the 15-min data intervals for PFISR density data. In addition, AE index is a standard tool that is used for identifying the events of interest.

Figure 4.2 illustrates the zero epoch selection and SEA implementation used. In Figure 4.2b, colored lines represent the AE index variations for individual events at 1-min resolution, shifted to zero epoch based on the time when a rapid increase in AE was observed. The bold black line is the resulting superposition of the individual AE variations, with the grey bars in Figure 4.2b showing the standard deviations for each 1 min.

In addition to the AE index data, the PFISR E-region electron density data were employed in this project. In particular, these data were integrated over the E-region range of altitudes up to 150 km to yield the E-region electron content estimates, $ITEC_{150}$, as described in Section 3.1. Because of much cruder time resolution for the PFISR data, the

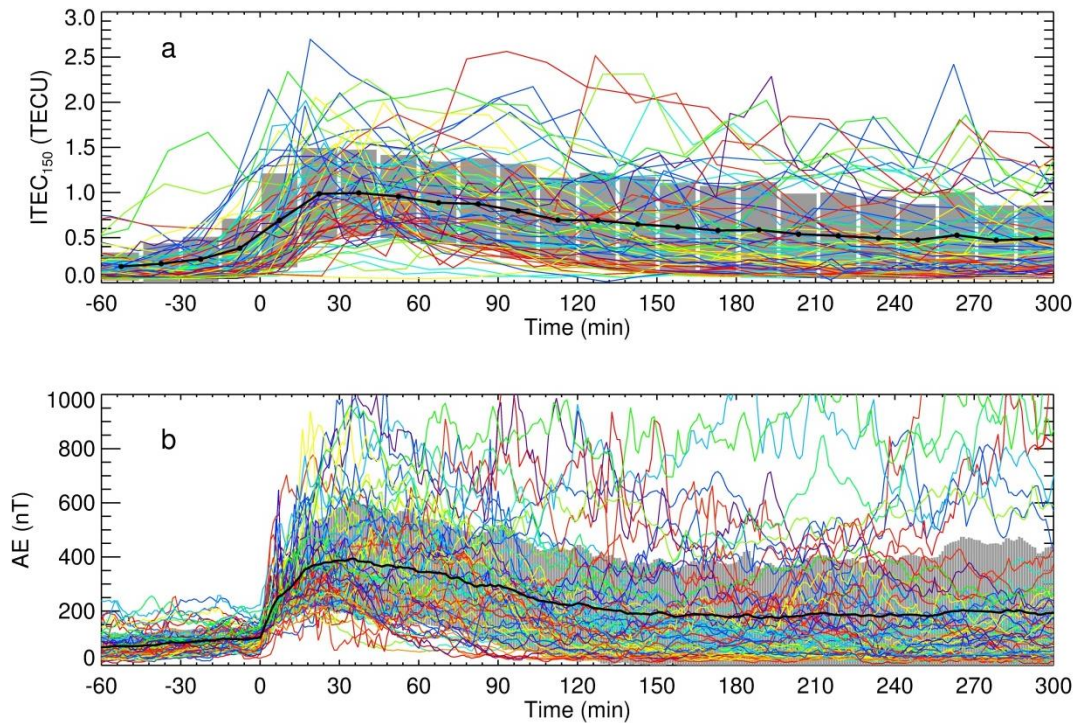


Figure 4.2: Superposed epoch analysis. Shown are (a) E-region electron content ITEC₁₅₀ and (b) AE index. Individual events are shown by the colored lines. The bold black line shows the mean values while grey bars indicate standard deviations.

ITEC₁₅₀ data were rarely aligned with zero epoch time from AE index. Thus, the ITEC₁₅₀ values were shifted not to zero epoch exactly (within 1 min) but to the closest boundary of 15-min interval. By doing this, it was ensured that all ITEC₁₅₀ measurements were aligned with each other and could be averaged. In Figure 4.2a, the ITEC₁₅₀ values for individual events (colored lines) are plotted with respect to zero epoch. Superposed ITEC₁₅₀ is shown by the bold black line and standard deviations are shown by the grey bars.

The same SEA technique was applied to the AC electron density data in 4.5 km altitude bins. From the resulting SEA density dataset, the maximum electron density (NmE), the altitude of the maximum density (hmE), and the thickness of the E-layer were found as described below.

Figure 4.3 presents results of this analysis. The SEA results are shown for (a) AE index, (b) PFISR electron density, (c) E-region electron content ITEC₁₅₀, (d) E-region

peak density, and (e) E-region thickness. The AE and $ITEC_{150}$ values were obtained as described above and are the same as in Figures 4.2a and b, respectively. NmE was determined for each density profile and these values are shown in panel (d). The hmE was found using two methods. First, the altitude was found at which the E-region peak density was reached; these values are shown by the red curve in Figure 4.3b. Second, the quadratic function was fitted to the obtained peak altitude and two points on the either side of it and the peak altitude of this fitted function was calculated; this 3-pt interpolated peak altitudes are shown by the black line in Figure 4.3b. The fitted function yields a better representation of time variation of hmE , resulting in a smooth trend rather than the step-like trend from the raw data. E-region thickness in panel (e) was determined by first finding NmE and hmE and then finding the altitude on either side of the peak where density was reduced to 75% of the maximum value. The difference between the two altitudes results in the thickness. Thickness was determined using raw data (red line) as well as 3-pt (yellow), 5-pt (blue), and 7-pt (black) interpolations that were performed as described above.

The AE index variation in Figure 4.3a shows a well-defined sharp onset at zero epoch that is shown by the dashed vertical line in all panels. This is, of course, not surprising since zero epoch was selected from all individual AE variations that exhibited this well-defined onset. In the SEA data, AE maintains a value of approximately 75 nT, increasing slightly upon approach to zero epoch. AE reaches its peak value of roughly 400 nT at 30 min after onset. At 300 min after onset, AE reduces to half of maximum.

In Figure 4.3c, $ITEC_{150}$ begins to rise before onset, doubling from 0.2 TECU to 0.4 TECU in the hour prior to onset. The maximum in $ITEC_{150}$ occurs 15–30 min after onset with a value of approximately 1 TECU. After the peak, $ITEC_{150}$ begins to reduce at about the same rate until it levels off during the last plotted hour with a value of roughly 0.5 TECU. In Figure 4.3b, the SEA of the electron density shows that, before onset, low densities (dark blues) were observed at all altitudes. On approach to onset, however, the density begins to increase slightly at mid and upper altitudes of the E-region (lighter

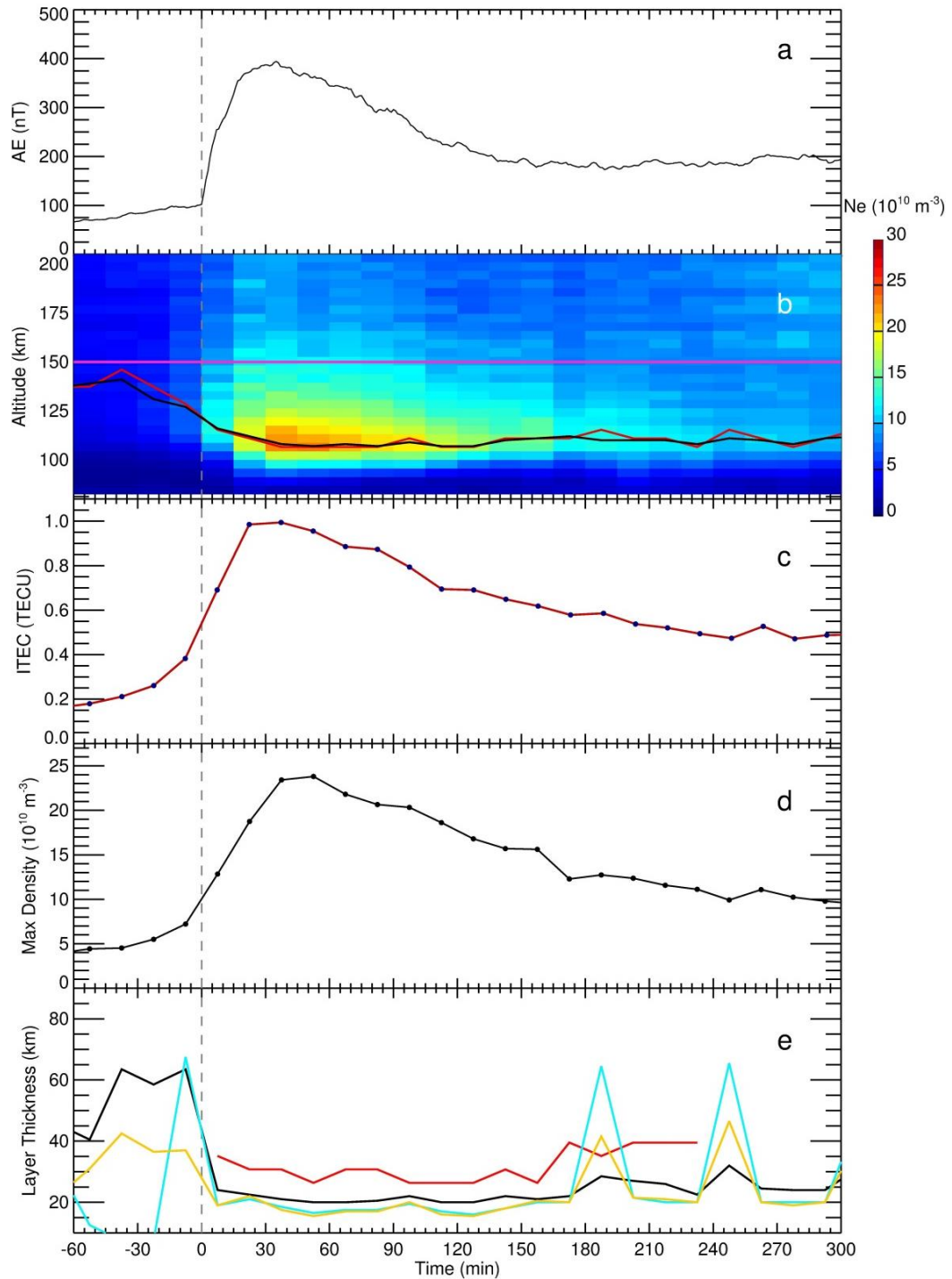


Figure 4.3: Superposed epoch analysis of nighttime disturbances. Shown are (a) AE index value, (b) PFISR electron density data, and (c) E-region electron content $ITEC_{150}$. In panel (b) the red (black) line indicates the altitude of maximum electron density based on raw (3-pt interpolated) data below the $ITEC_{150}$ ceiling (pink line). Panels (d) and (e) show the maximum E-region density and (e) thickness of E-layer using the raw data (red), 3-pt interpolation (yellow), 5-pt interpolation (blue), and 7-pt interpolation (black).

blues). Immediately after onset, the density increases dramatically, reaching a peak concentration and spread in the 30–60 min time block, as indicated by the yellow and orange colors of the plot cells. The extent and intensity of the increased density gradually tapers off as time passes. Light and medium blues dominate the plot once again three hours after onset, though no altitude returns to the dark blue color of the low densities pre-onset.

The hmE also shown in Figure 4.3b is near the ceiling of the region of interest, 82–150 km, prior to onset. The hmE decreases until it reaches approximately 110 km, 30 min after onset. It remains at this altitude until ~135 min after onset, after which point it rises to ~115 km for two hours before decreasing slightly once more.

In Figure 4.3d, NmE increases gradually prior to onset, staying in near $5 \times 10^{10} \text{ m}^{-3}$. Immediately following onset, there is a sharp rise in the peak density. The greatest electron density occurs in the 45–60 min period with a value of $24 \times 10^{10} \text{ m}^{-3}$. NmE decreases after that until it reaches approximately $10 \times 10^{10} \text{ m}^{-3}$, 300 min after onset.

In Figure 4.3e, the E-layer thickness is high (50 km) prior to onset based on the interpolated data. The raw data does not decrease to 75% within the E-region and thus no estimate (red line) is obtained until after onset. After onset, the layer thickness decreases to 20–30 km for 150 min before gradually increasing by the end of the plotted timespan. The thickness as defined by the raw PFISR data, once again, is undetermined by 240 min after onset.

Overall, there are three phases visible in Figure 4.3: pre-onset (from –60 to 0 min), the main ionospheric response (0 to 45–60 min), and recovery (from 45–60 min onwards). Figure 4.3 shows that during pre-onset, the E-region begins to display gradually increasing density levels as onset is approached. While a layer is not yet well defined, hmE begins to lower in advance of onset. Immediately following onset, the main response of the E-region shows a rapid increase in AE, NmE, and ITEC_{150} with further lowering of hmE. Peak values for AE, NmE, and ITEC_{150} are all reached during this period. A thick layer develops, narrowing slightly during the main response before reaching a more stable thickness. After the main response, a gradual decrease in AE,

NmE, and $ITEC_{150}$ occurs during recovery. The rate of decrease in NmE and $ITEC_{150}$ reduces until both remain relatively constant. As recovery progresses, the density intensity weakens with the layer thickness gradually widening as a result. During this period, hmE rises slightly for approximately 90 min before lowering once again.

Finally, it is apparent from several of the panels in Figure 4.3, most notably panel (b), that there is a background contribution to the data attributable to diurnal variance. For example, the upper altitudes in the density plot (Figure 4.3b) begin to fade to a darker blue 90 min after onset, indicating a decrease in density, but do not reduce to pre-onset levels before once again increasing 180 min after onset. Shortly after, there is a visible increase in the electron density at altitudes bordering and entering the E-region. This is a signature of the diurnal variation. Even though the onset times were not all the same, they were predominantly in the midnight sector around 11 UT (00 MLT), which means that some background diurnal variation was present in the SEA values for all parameters of interest. One possible consequence of this “contamination” is that all parameters did not go down to their initial, pre-onset values, even after 300 min after onset. Thus, to acquire a more accurate picture of the behavior of the electron density and other derived parameters solely due to the auroral events, the background contribution must be removed.

4.2 Quiet-Time Background Contribution

In order to determine background contribution, undisturbed (quiet) days were found first. For days to be considered quiet, the AE values throughout the day were required to display a roughly steady behavior. Short-duration increases of up to 100 nT were allowed to maximize the number of quiet days. In addition, quiet nights required a minimum of 8 consecutive hours of AC density data from PFISR during nighttime. Furthermore, the days chosen had to be representative of the time of year from where disturbed periods originated. Where available data allowed, quiet nights were chosen as near as possible to a disturbed night in the same month and year.

The SEA results for all selected quiet days are displayed in Figure 4.4. The zero epoch times used here were the same as those in the SEA of all disturbed events, Figure

4.3. That is, for each disturbed event with a particular onset time, one quiet day was selected and in the SEA technique the times for the quiet day was shifted to that onset time. The use of only one quiet day per disturbed event in analysis was made as fully quiet days within the same month display no significant variation. Quiet days chosen for this analysis were within this range for their corresponding disturbance. Since SEA results for E-layer thickness showed similarly poor-quality results to those obtained in SEA of disturbed events prior to onset and 240 min after the onset, i.e. no estimates using “raw” data and highly variable values for interpolated data, these results are not presented here.

The AE index maintains a value of ~ 40 nT throughout the entire time period. The relatively flat AE variation and a small value are expected for quiet days and this indicates that our selection of quiet-time periods was reasonably good. Electron densities shown in Figure 4.4b, unlike AE in panel (a), exhibit a diurnal variation. Photoionization and other processes occur during daylight hours that raise the density values. Due to the distribution of disturbance onsets, the zero epoch was primarily near 11 UT with most events found in spring or autumn. Sunrise in spring and autumn happens between 14–17 UT, which corresponds to 180–360 min after onset on average, which overlaps significantly with the plotted time span in Figure 4.4. This means diurnal variation has an impact on the quiet-time SEA results displayed in Figure 4.4b. In the SEA of densities plotted in Figure 4.4b, these diurnal effects are evident as a lightening of the shade of blue, particularly in the top-right corner of the plot. The higher altitudes, where photoionization begins earlier in the day, see an increase in density before the lower altitudes. While not a dramatic change (the color scale was kept consistent with that Figure 4.3), the effect reaches into the E-region during the later part of the timespan plotted, visible as a medium rather than dark blue. The density distribution in the E-region during quiet times is such that hmE is always at the top of the region, as shown by the red line in Figure 4.4b. Without any sort of disturbance at night, there is no mechanism to cause ionization at lower altitudes, thus electron density in the E-region is greatest at the top of the altitude range considered; 82–150 km.

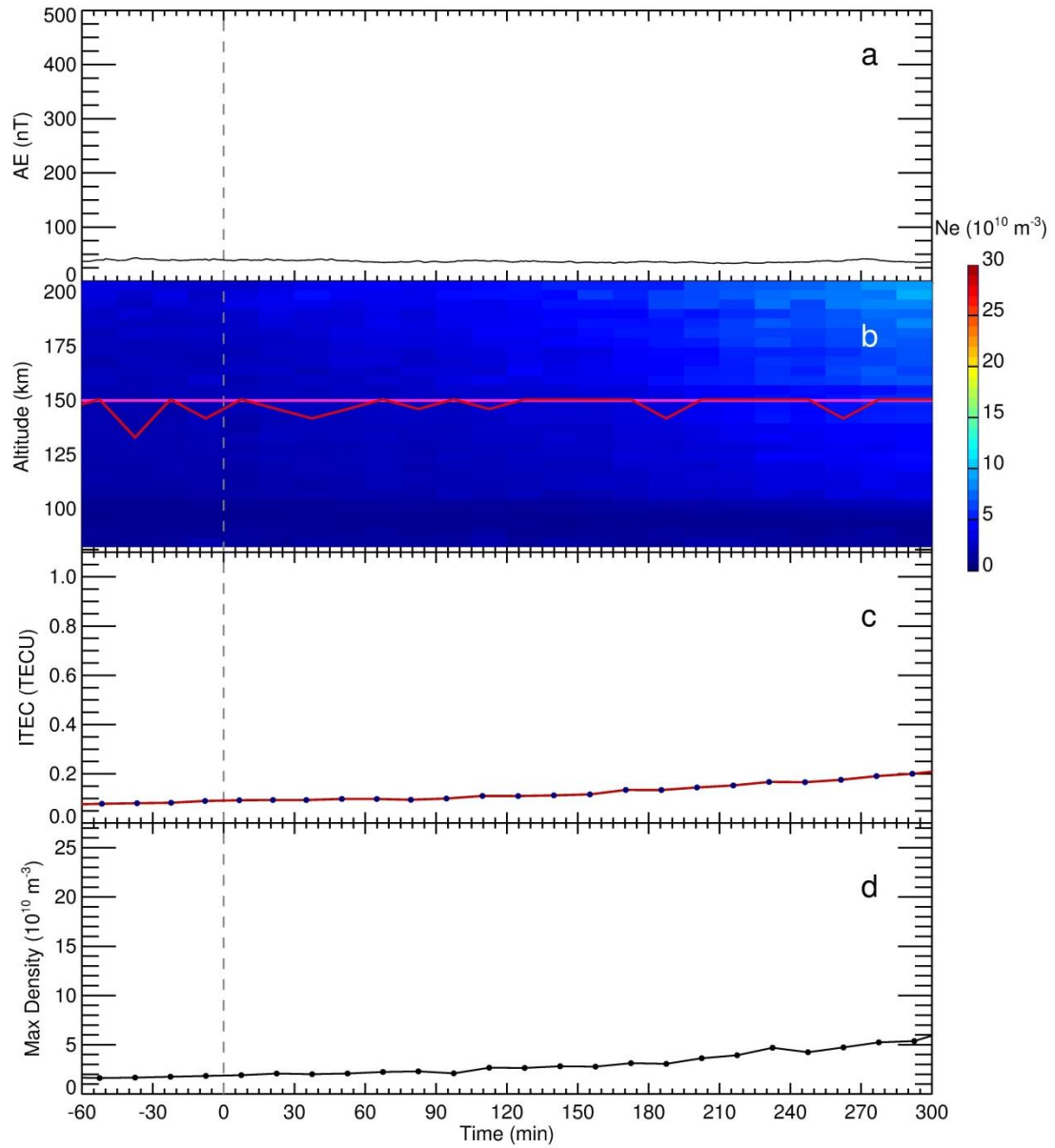


Figure 4.4: SEA results for quiet nights. The format is the same as for the first 4 panels of Figure 4.3. The E-layer thickness results are not presented here as explained in the text.

The $ITEC_{150}$ values from quiet-time SEA are displayed in Figure 4.4c. At 60 min before zero epoch, the E-region electron content is very small, ~ 0.08 TECU. For the first three hours of the plot, there is a slight rise in $ITEC_{150}$, though it does not exceed 0.1 TECU. After the initial three hour time span, $ITEC_{150}$ begins to increase at a faster rate until it ends at approximately double the value at which it started (0.2 TECU). The increase in $ITEC_{150}$ is due to the diurnal variation visible in Figure 4.4b. Finally, the NmE displayed in Figure 4.4d also shows the diurnal effects. This peak density is observed at the top of the altitude range for the entire time span. At 60 min before zero epoch, NmE is approximately $2.0 \times 10^{10} \text{ m}^{-3}$. By the end of the time span, NmE triples in value.

Overall, Figure 4.4 shows that there is diurnal variation present in the set of quiet-time PFISR-derived values, indicated by the gradual increase in density and $ITEC_{150}$ values. Additionally, the steady and low values in each plot show that there are no other significant sources of variations.

4.3 SEA with Quiet-Time Contribution Removed

As mentioned at the end of Section 4.1, in order to get a more accurate picture of variations during disturbed periods, the quiet-time variations must be removed from the disturbed-period data. In this section, the SEA results from two different methods of this removal are presented. In the first method, the quiet-time variations determined as described in the previous section were subtracted from the data collected during disturbed times. The resulting data is then free of potential contamination from diurnal effects, allowing for emphasis of the perturbations caused by auroral activity only. The second method used the percent difference between the disturbed and quiet-time datasets.

The SEA of perturbations in AE index and PFISR electron density was carried out by taking the average quiet-time AE and density data from SEA presented in Figures 4.3a and b and subtracting it from the corresponding disturbed data values shown in Figures 4.2a and b. This approach is equivalent to doing subtraction first for each individual event and averaging second, as long as shifting to zero epoch is done before everything else, since the average of differences is equal to the difference of averages. These results are presented in Figure 4.5a and b. The remaining three panels of Figure 4.5 are based on the

density perturbation data shown in Figure 4.5b. These values were calculated using the same approach as that used to obtain the data shown previously in Figures 4.3c–e. As there is no variation present in the quiet-time AE readings, Figure 4.4a, subtracting them from the AE of disturbances only serves to reduce the entire dataset by a ~ 40 nT value, Figure 4.5a. However, even with this correction, the AE does not start at zero before onset time. This suggests that auroral disturbances have a slightly elevated AE index signature before the main onset.

The perturbation electron density shown in Figure 4.5b displays a more narrow altitude range where density is enhanced, as compared to Figure 4.3b. This altitude range also becomes more narrow as time from onset increases. The perturbation density reaches its peak between 30–60 min after onset at an altitude of ~ 115 km (orange plot cells). While previously masked by the diurnal variation, it is more apparent in this analysis that the electron density begins to fade in magnitude and altitude coverage with time from onset increasing. The E-region peak density is reached between 110–120 km in altitude as indicated by the red (black) line representing the raw (3-pt interpolated) altitude of peak density. Similarly to the dataset presented in Figure 4.3, hmE decreases both prior to and shortly after onset, but then after approximately 2 hours it rises for 45 min before dropping back down to a lower altitude, indicating that this behavior is not caused by the diurnal effects.

The perturbation in the E-region electron content $ITEC_{150}$ displayed in Figure 4.5c, similarly to AE, does not start from zero before onset. This means that electron content in the E-region is already increasing gradually before onset and this is not due to diurnal variation. The peak content occurs between 15–45 min after onset with a value of approximately 0.9 TECU. After 45 min, the electron content starts to decrease. However, the perturbation electron content drops off faster as compared with the $ITEC_{150}$ itself since its (increasing) diurnal component has been removed.

The perturbation NmE is displayed in Figure 4.5d. Similarly to electron content, with quiet-time contribution removed, the rate at which it decreases is greater than in the

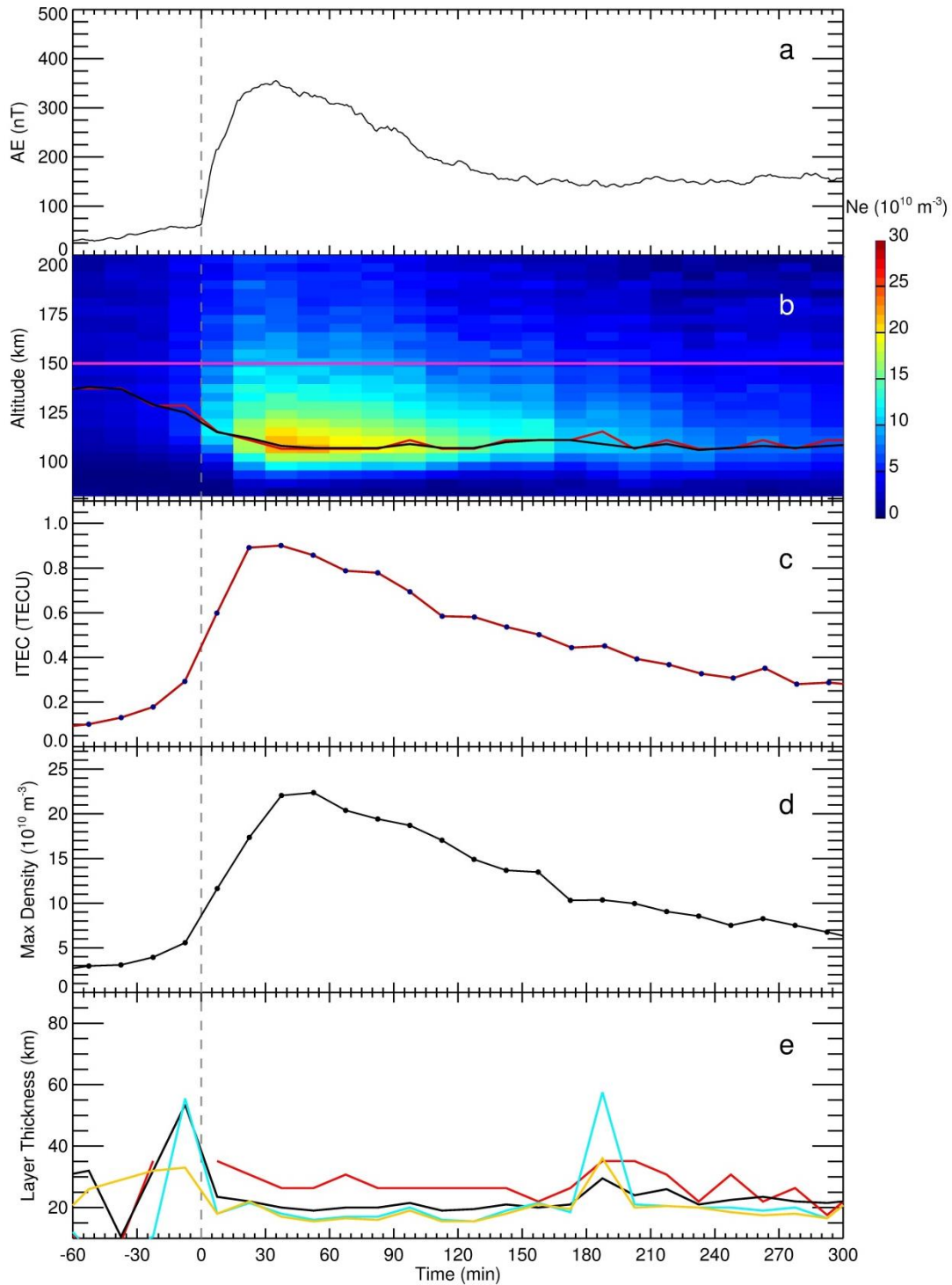


Figure 4.5: SEA of perturbations. The same as Figure 4.3, but for perturbations.

dataset presented in Figure 4.3d. The peak density values occur between 30–60 min after onset.

The E-layer thickness for the perturbation density values initially displays a similar behavior to the values presented in Figure 4.3e. That is, before onset, the layer is relatively thick and then it rapidly narrows to a width of approximately 20 km. However, as time passes, the layer thickness with quiet-time density removed increases to a lesser degree than in Figure 4.3e, with the 3-pt and 5-pt interpolation remaining nearly steady. Thickness based on raw PFISR data is no longer undefined after 240 min and displays a similar trend as the interpolated data-sets.

Overall, Figure 4.5 shows that pre-onset levels of AE, NmE, and $ITEC_{150}$ are greater than that during quiet-times. Removing diurnal contribution had no discernible effect on the pre-onset behavior trend observed in Figure 4.3, merely reducing overall values by a specific amount. The same is true for the response period; while the values are modestly lower, the E-region still displays a rapid increase in AE, NmE, and $ITEC_{150}$ with the lowering of hmE and appearance of a thick layer. During recovery, $ITEC_{150}$ and NmE decrease at a steady and greater rate with diurnal contribution removed though do not return to pre-onset levels. During perturbation recovery, hmE still displays a slight rising and later lowering. Finally, layer thickness widens slightly over time.

The approach used to obtain perturbation values displayed in Figure 4.5 is reasonably successful in removing diurnal contributions. However, the perturbations or differences with respect to the quiet-time values are measured in absolute values (nT, TECU, etc) without accounting for the fact that quiet-time values themselves change, however slightly, with time of the day. Thus perturbations of say 1 TECU observed at 0 and 300 min from onset are the same in absolute terms, but different in relative terms when calculated with respect to quiet-time variation as a ratio or percentage (it is larger at 0 min when quiet-time values are smaller).

In order to consider this relative variation, the percent difference relative to quiet-time was calculated for the AE and density values. Figure 4.6 displays the results of this “relative perturbation” analysis. The format of the figure panels is the same as in the

previous figures, but one should also note differences in the maximum scales that reach 1100%. As in Figure 4.4, the layer thickness is omitted from Figure 4.6, since there is no layer thickness to compare to during quiet times.

The percent difference in AE, Figure 4.6a, peaks at ~30 min after onset with a value that is a full order of magnitude larger than during quiet times. An hour before onset, the difference in AE is approximately equal the quiet-time value (100%) which is equivalent to AE index itself being twice that on the nights of disturbance, increasing to two and a half times (150% for the difference) just before onset.

Figure 4.6b displays the percent difference in electron density. Above the E-region (above the pink line), there is little percent difference outside of the first 90-min window after onset. This is to be expected in the case when contributions to electron density are solely due to diurnal variations. In the E-region, the maximum percent difference in electron density for the entire night occurs in the 30–45 min time period (yellow cells in the plot) at an altitude of ~100 km. This particular altitude and time period has slightly more than an order of magnitude difference from quiet times. During the most disturbed period (0–3 hours), most altitudes and time blocks are colored in shades of blue, indicating approximately a single order of magnitude increase over quiet times.

The raw and interpolated height data values are in close agreement for the time period of interest. Even long after zero epoch, the altitude of greatest percent difference in electron density decreases. For 3 hours after onset, it maintains an altitude of approximately 100 km; it then drops to roughly 95 km for 90 min, and then further drops to 90 km for the remainder of the data set. This is in contrast to the other two approaches presented in Figures 4.3b and 4.4b, where the peak altitude showed some variation.

The percent difference in ITEC_{150} is displayed in Figure 4.6c. Before onset, values of up to five times are observed relative to the quiet-time values. The percent difference in ITEC_{150} follows the density plot; it appears 30–45 min after onset with a peak value that is an order of magnitude greater relative to quiet-time values.

The percent difference of the peak densities is displayed in Figure 4.6d. The largest value of the difference occurs in the same 30–45 min time period as in the previous two

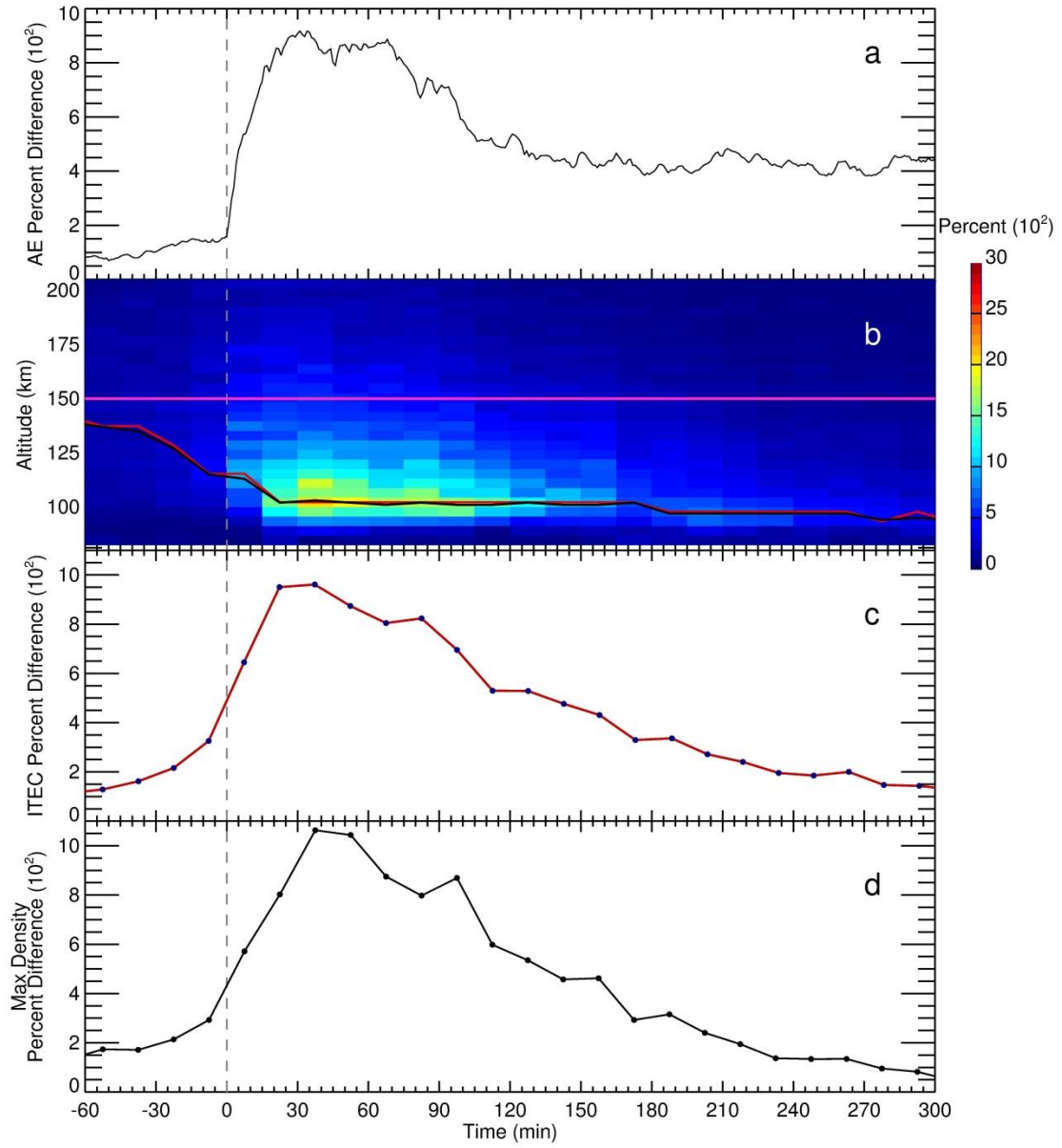


Figure 4.6: Normalized SEA perturbations. The same as Figure 4.4 but for normalized perturbations (see text for details).

panels, with a value that is an order of magnitude greater than that during quiet times. After 45 min, the percent difference has a general trend of decrease until the peak density is approximately twice as large as that during quiet times.

4.4 Discussion and Summary

In this project, superposed epoch analysis was performed using the PFISR data during selected periods of auroral activity from March 2007 through April 2011 in order to investigate the E-region response to and evolution during auroral disturbances. The nighttime E-region density dynamics were predominantly studied in the past on a case-by-case basis with majority of previous ISR investigations focusing on thin Es layers, Section 1.2.2. The presented statistical investigation of thick auroral E-layers thus makes an important step towards better characterization of E-region density at auroral latitudes, which is important for improving ionospheric models such as IRI. At the same time, the observed features in $ITEC_{150}$, NmE, and hmE also give us important insights into particle spectra behavior and evolution of auroral forms during auroral events.

The auroral events were defined as described in Section 4.1, with the total of 65 events used in the analysis. Quiet-time periods were also chosen to compare with disturbed events and to remove diurnal effects. Of particular interest to this study was the behavior of the full electron density profile, the behavior of the E-layer, and the implied behavior of particle precipitation spectra throughout various stages of auroral disturbances.

The first interesting result of the SEA analysis was that there were three discernible phases in the E-region response to auroral events: pre-onset, the main response, and recovery. These three phases were seen in the initial SEA of events, Figure 4.3, as well as in the SEA with quiet-time diurnal variation removed, Figure 4.5. Pre-onset was seen in Figures 4.3b and 4.5b, at -60–0 min, in the form of low electron densities (dark blue) throughout the E-region gradually increasing toward zero epoch (lighter blue). The main response was seen as a rapid increase in electron density (light blue to yellow and orange) throughout the E-region between 0–45 min. Recovery was seen from 60 min onward with

a steady decrease in electron density (return to light and dark blues) throughout the E-region.

Each of these three phases was generally characterized by distinct trends in “integral” characteristics of density profiles $ITEC_{150}$, NmE, and hmE. During pre-onset, AE, $ITEC_{150}$, and NmE were observed to display a slight rise in both Figures 4.3 and 4.5. During the main response, the same three variables were seen to increase rapidly and level off at a peak value. During recovery phase, AE, $ITEC_{150}$ and NmE were seen to decrease, though the rate and duration of the decrease was greater with quiet-time variation removed, Figure 4.5, than in the initial SEA analysis, Figure 4.3. This is because quiet-time densities were increasing towards the end of the period of interest and so their removal effectively lowered the trends. During pre-onset, hmE was seen near the top of the E-region altitude range 90–150 km in both Figures 4.3 and 4.5, gradually lowering with onset approaching. In the main response, hmE was observed to lower rapidly and then maintain roughly the same altitude during early recovery phase. During late recovery starting at ~2 hours after onset, hmE was seen to rise slightly for ~1 hour before it returned a lower altitude ~3 hours after onset. Throughout the 1-hour period where the rise in hmE was observed, the trends that were observed in the other measured variables did not change much.

A study by Jones *et al.* [2009] provided one possible explanation for the observed rise in hmE. They used PFISR to observe pulsating aurora events and found that in three of their four events, hmE displayed a rise towards the end of an event. The auroral events chosen for the current study were not distinguished by type and the hmE rise found here was temporary, i.e. hmE showed a decrease at ~3 hours after onset. Nevertheless, the two features may be related and rise in hmE may therefore be attributed to an inclusion of some pulsating aurora events in the current dataset.

The final group of results of interest was the implied behavior of the particle precipitation spectra that can be inferred from trends of peak density, layer thickness, and peak height. After onset, the development of the auroral layer implies that particle flux was increasing. That the layer developed in the E-region suggests the energy was

relatively high. That the layer itself was thick, 20–30 km, suggests that the energy spectrum was relatively broad.

Figures 4.3e and 4.5e displayed slightly different behavior at the end of the plotted timespan. Whereas Figure 4.3e displayed an increase in layer thickness, Figure 4.5e did so to a lesser degree and ended with a layer thickness nearly identical to that of the main response and early recovery phases. Given that removal of diurnal contribution had a greater effect on the electron density in higher altitudes over time and that the lower altitudes experienced little to no increase in density during disturbances, these features were perhaps not unexpected. A progressively stronger reduction in the electron density was observed with time from onset increasing. At the same time, a progressively greater contribution from diurnal variation was also observed, with stronger diurnal effects at the higher altitudes of interest, Figure 4.4b. Removal of the diurnal contribution effectively reduced the electron density and this reduction was stronger at higher altitudes. This likely had the effect of reducing the layer width in Figure 4.5e as compared to Figure 4.3e. The behavior of the layer thickness suggests that the precipitating particle spectra became only slightly broader, though spectra were still centered at high energies as hmE was still well within the E-region.

There have been a number of prior studies which investigated different aspects of auroral events and the particle precipitation spectra involved [*Bates and Hunsucker, 1974; Hunsucker, 1975; Strickland et al., 1983; Jones et al., 2009*]. The studies by *Bates and Hunsucker [1974]* and *Hunsucker [1975]* are related, since both used the Chatanika ISR to probe the high-latitude E-region under various conditions. From these two studies, it was seen that the E-layer due to auroral precipitation was thick with the particle energy around 5 keV. While neither study explicitly explored the evolution of layer thickness or hmE during an auroral event, the hmE observed was approximately in the same altitude range as seen in the current analysis during the bulk of the recovery phase. *Strickland et al. [1983]* explored the plasma density profile and precipitating electron spectrum during diffuse and discrete aurora, using a chemistry-based model with a Maxwellian distribution for diffuse aurora and Gaussian distribution for discrete. For the altitude in

the E-region that corresponded to the hmE value observed in the current analysis, *Strickland et al.* [1983] estimated the energies involved in the precipitating particles to be 5–7.5 keV depending on the type of aurora involved. The study by *Jones et al.* [2009] estimated layer thicknesses during pulsating aurora to be 15–25 km. By using an inversion technique on PFISR density, they then estimated the precipitating electron energies, with the primary spectral peak at 6 keV and the bulk contribution from particles under 12 keV. In comparison to these prior studies, the hmE and layer thickness observed in the current study were similar. Therefore, the energies of precipitating particles are also likely to be comparable.

Figure 4.7 summarizes the above observations of E-region characteristics and their implications by showing the energy spectra during each of the three response phases. In this presentation, the information about the height of the spectrum (i.e. vertical extent) or total particle flux is based on the E-region peak density and electron content. The average or peak energy (i.e. horizontal position) is based on peak height, whereas the spectral width is based on E-layer thickness. Before onset (blue), the spectrum is broad, its average energy is relatively low, and so is the total flux. At the peak of the main response (red), the precipitating particles have hardened considerably with the main peak to be likely near 6 keV based on information from prior studies. The narrower E-layer in this stage implies narrower energy spectrum, while the large increase in $ITEC_{150}$ implies a

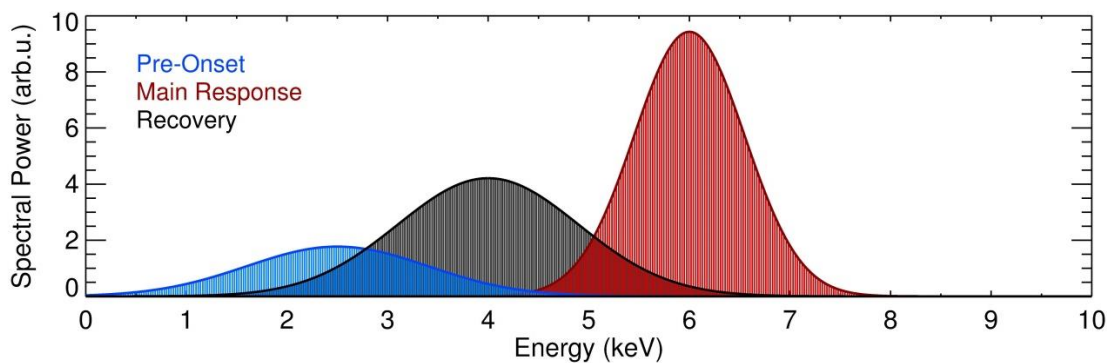


Figure 4.7: A sketch of particle precipitation spectra during E-region response phases. Shown are the energy spectra during the 3 phases of E-region response: pre-onset (blue), the main response (red), and recovery (black). The 3 spectra shown here are based on the nighttime E-region behavior during auroral disturbances.

much greater flux. During recovery (black), the spectra soften and become broader. The decline in ITEC_{150} throughout the recovery phase suggests a smaller flux than during the main response, but as ITEC_{150} does not completely return to pre-onset levels, it also suggests that particle flux is somewhat greater than before onset.

5. Conclusions

In this thesis, the dynamics of the high-latitude nighttime E-region have been investigated using a number of methods in order to better understand the relationship between the E-region electron density and auroral activity as well as to characterize and quantify the evolution of auroral events using their E-region density signatures. Plasma density structures within the ionosphere affect radio wave propagation and as such understanding the behavior in the ionospheric E-layer during auroral events becomes important. While many past studies focused on thin Es phenomena, the dynamics of thick auroral layers have been less investigated and this thesis focuses on two aspects of this phenomenon as described below.

The relationship between electron density and auroral activity was investigated statistically in Section 3 by analyzing correlations between the magnetic Auroral Electrojet index and E-region electron content estimated from the PFISR electron density data at 4.5-km height resolution. Correlation analysis was conducted for various periods throughout the day and seasons as well as for different Solar Zenith Angle conditions to better understand the complex interplay between solar and auroral effects. It was found that AE index and E-region electron content exhibited significant positive correlation, with greater correlation occurring near local magnetic midnight. Seasonally, summer had the lowest correlation values while spring and autumn were comparable. The midnight feature was interpreted as an indication that the electrojet system near magnetic midnight is mostly controlled by electric conductance. Additionally, E-region contribution to TEC was estimated and investigated systematically for the first time. While during quiet times this contribution was found to be quite small (~5%), during active periods this contribution was found to be 30% of the PFISR-derived TEC estimates, which, by comparison to previous PFISR/GPS TEC studies, implied a contribution of approximately 22.5% to GPS-derived TEC. This finding emphasized the need for better characterization of the nighttime E-region at auroral latitudes, particularly within the current ionospheric models such as IRI or STORM-E.

The response of nighttime E-region to auroral disturbances was examined in Section 4 using the superposed epoch analysis technique applied to the PFISR electron density data. In this project, the behavior of the full density profile was considered versus time from disturbance onset, along with several integral characteristics of the E-region such as its electron content, peak density, peak height, and layer thickness. Overall, three phases were discernible in the E-region response: pre-onset, the main ionospheric response, and recovery. Pre-onset was characterized by low values in most considered parameters which increased slightly as zero epoch was approached except for the peak height which was near the top of the considered E-region altitude range of 90–150 km. The main response was marked by a sharp increase in peak density and electron content and lowering of peak height. Finally, recovery was characterized by a steady decrease in electron content and peak density, while peak height primarily remained steady. The above-described behavior of the E-region density signatures implies that energy spectra of precipitating electrons evolve in a particular way during auroral disturbances. Initially broad and soft spectra narrow and harden during the main response, which is followed by gradual softening and broadening during recovery.

References

- Appleton, E.V., On some measurements of the equivalent height of the atmosphere ionised layer, *Proc. R. Soc. Lond. A*, *126*, 542–569, 1930.
- Appleton, E.V., and Naismith, R., Some further measurements of upper atmospheric ionization, *Proc. R. Soc. Lond. A*, *150*, 685–708, 1935.
- Baker, J.B., Greenwald, R.A., Ruohoniemi, J.M., Oksavik, K., Gjerloev, J.W., Paxton, L.J., and Hairston, M.R., Observations of ionospheric convection from Wallops SuperDARN radar at midlatitudes, *J. Geophys. Res.*, *112*, A01303, doi:10.1029/2006JA011982, 2007.
- Bates, H.F., and Hunsucker, R.D., Quiet and disturbed electron density profiles in the auroral zone ionosphere, *Radio Sci.*, *9*, 455–467, 1974.
- Beynon, W.J.G., and Brown, G.M., Region-E and solar activity, *J. Atmos. Terr. Phys.*, *15*, 168–174, 1959.
- Beynon, W.J.G., and Williams, P.J.S., Incoherent scatter of radio waves from the ionosphere, *Rep. Prog. Phys.*, *41*, 909–956, 1978.
- Bilitza, D., *International Reference Ionosphere: IRI-90*, National Space Science Data Center, Rep. 90-22, Greenbelt, Maryland, 1990.
- Bilitza, D., International Reference Ionosphere 2000, *Radio Sci.*, *36*, 261–275, doi:10.1029/2000rs002432, 2001.
- Bilitza, D., and Reinisch, B.W., International Reference Ionosphere 2007: improvements and new parameters, *Adv. Space Res.*, *42*, 599–609, doi:10.1016/j.asr.2007.07.048, 2008.
- Bowles, K.L., Observation of vertical-incidence scatter from the ionosphere at 41 Mc/sec, *Phys. Rev. Lett.*, *1*, 454–455, 1958.
- Bristow, W.A., Ruohoniemi, J.M., and Greenwald, R.A., Super Dual Auroral Radar Network observations of convection during a period of small-magnitude northward IMF, *J. Geophys. Res.*, *103*, 4051–4061, doi:10.1029/97JA03168, 1998.
- Bristow, W.A., Yee, J.H., Zhu, X., and Greenwald, R.A., Simultaneous observations of the July 1996 2-day wave event using the Super Dual Auroral Radar Network and the high resolution Doppler imager, *J. Geophys. Res.*, *104*, 12,715–12,721, doi:10.1029/1999JA900030, 1999.
- Buneman, O., Scattering of radiation by the fluctuations in a nonequilibrium plasma, *J. Geophys. Res.*, *5*, 2050–2053, 1962.
- Chapman, S., The absorption and dissociative or ionization effect of monochromatic radiation in an atmosphere on a rotating Earth, *Proc. Phys. Soc.*, *43*, 26–45, 1931.

- Chisham, G., and Freeman, M.P., A reassessment of SuperDARN meteor echoes from the upper mesosphere and lower thermosphere, *J. Atmos. Terr. Phys.*, *102*, 207–221, doi:10.1016/j.jastp.2013.05.018, 2013.
- Conde, M., and Smith, R.W., Phase compensation of a separation scanned, all-sky imaging Fabry-Perot spectrometer for auroral studies, *Appl. Opt.*, *36*, 544–5450, doi:10.1364/ao.36.005441, 1997.
- Coyne, T.N.R., and Belrose, J.S., The diurnal and seasonal variation of electron densities in the midlatitude D region under quiet conditions, *Radio Sci.*, *7*, 163–174, 1972.
- Davies, J.A., and Lester, M., The relationship between electric fields, conductances and currents in the high-latitude ionosphere: a statistical study using EISCAT data, *Ann. Geophys.*, *17*, 43–52, doi:10.1007/s00585-999-0043-3, 1999.
- Davis, T.N., and Sugiura, M., Auroral electrojet activity index AE and its universal time variations, *J. Geophys. Res.*, *71*, 785–801, 1966.
- Evans, J.V., Theory and practice of ionosphere study by Thomson scatter radar, *Proc. IEEE*, *57*, 496–530, 1969.
- Farley, D.T., Incoherent scatter power measurements; a comparison of various techniques, *Radio Sci.*, *4*, 139–142, 1969.
- Fejer, J.A., Radio-wave scattering by an ionized gas in thermal equilibrium, *J. Geophys. Res.*, *65*, 2635–2636, 1960.
- Forbes, J.M., The equatorial electrojet, *Rev. Geophys. Space Phys.*, *19*, 469–504, doi:10.1029/RG019i003p00469, 1981.
- Golden, D. I., Spasojevic, M., Li, W., and Nishimura, Y., An empirical model of magnetospheric chorus amplitude using solar wind and geomagnetic indices, *J. Geophys. Res.*, *117*, A12204, doi:10.1029/2012JA018210, 2012.
- Gordon, D.I, and Brown, R.E., Recent advances in fluxgate magnetometry, *IEEE Trans. Magn.*, 76–82, 1972.
- Gordon, W.E., Incoherent scattering of radio waves by free electrons with applications to space exploration by radar, *Proc. IEEE*, *46*, 1824–1829, 1958.
- Griffin, E.M., Aruliah, A., Müller-Wodarg, I. C. F., and Aylward, A.: Comparison of high-latitude thermospheric meridional winds II: combined FPI, radar and model Climatologies, *Ann. Geophys.*, *22*, 863–876, doi:10.5194/angeo-22-863-2004, 2004.
- Hall, G.E., MacDougall, J.W., Moorcroft, D.R., St-Maurice, J.P., Manson A.H., and Meek, C.E., Super Dual Auroral Radar Network observations of meteor echoes, *J. Geophys. Res.*, *102*, 14,603–14,614, doi:10.1029/97JA00517, 1997.
- Heinselman, C.J., and Nicolls, M.J., A Bayesian approach to electric field and E-region neutral wind estimation with the Poker Flat Advanced Modular Incoherent Scatter Radar, *Radio Sci.*, *43*, RS5013, doi:10.1029/2007RS003805, 2008.

- Hunsucker, R.D., Chatanika radar investigation of high latitude E-region ionization structure and dynamics, *Radio Sci.*, 10, 277–288, 1975.
- Hunsucker, R.D., and Hargreaves, J.K., *The High-Latitude Ionosphere and Its Effects on Radio Propagation*, Cambridge University Press, New York, 2003.
- Huuskonen, A., Nygrén, T., Jalonen, L., Bjorna, N., Hansen, T.L., Brekke, A., and Turunen, T., Composition in sporadic E layers measured by the EISCAT UHF radar, *J. Geophys. Res.*, 93, 1988.
- Jenkins, B., Jarvis, M.J., and Forbes, D.M., Mesospheric wind observations derived from Super Dual Auroral Radar Network (SuperDARN) HF radar meteor echoes at Halley, Antarctica: preliminary results, *Radio Sci.*, 4, 957–965, doi:10.1029/98RS01113, 1998.
- Jones, S.L., Lessard, M.R., Fernandes, P.A., Lummerzheim, D., Semeter, J.L., Heinselman, C.J., Lynch, K.A., Michell, R.G., Kintner, P.M., Stenbaek-Neilsen, H.C., and Asamura, K., PFISR and ROPA observations of pulsating aurora, *J. Atmos. Sol. Terr. Phys.*, 71, 708–716, doi:10.1016/j.jastp.2008.10.004, 2009.
- Kamide, Y. and Vickrey, J.F., Relative contribution of ionospheric conductivity and electric field to the auroral electrojets, *J. Geophys. Res.*, 88, 7989–7996, 1983.
- Kellerman, A.C., Makarevich, R.A., Honary, F., and Hansen, T.L., On the relationship between auroral absorption, electrojet currents, and plasma convection, *Ann. Geophys.*, 27, doi:10.5194/angeo-27-473-2009, 2009.
- Kivelson, M.G., and Russell, C.T., *Introduction to Space Physics*, Cambridge University Press, New York, 1995.
- Kustov, A.V., Papitashvili, V.O., Sofko, G.J., Schiffler, A., Feldstein, Y.I., Gromova, L.I., Levitin, A.E., Belov, B.A., Greenwald, R.A., and Ruohoniemi, M.J., Dayside ionospheric plasma convection, electric fields, and field-aligned currents derived from the SuperDARN radar observations and predicted by the IZMEM model, *J. Geophys. Res.*, 102, 24,057–24,067, doi:10.1029/97ja02309, 1997.
- Lehtinen, M.S., and Häggström, I., A new modulation principle for incoherent scatter measurements, *Radio Sci.*, 22, 625–634, doi:10.1029/RS022i004p00625, 1987.
- Lilensten, J., and Cander, Lj.R., Calibration of the TEC derived from GPS measurements and from ionospheric models using the EISCAT radar, *J. Atmos. Sol. Terr. Phys.*, 65, 833–842, doi:10.1016/S1364-6826(03)00087-7, 2003.
- Makarevich, R.A., and Nicolls, M.J., Statistical comparison of TEC derived from GPS and ISR observations at high latitudes, *Radio Sci.*, 48, 441–452, doi:10.1002/rds.20055, 2013.
- McWilliams, K. A., Pfeifer, J. B., and McPherron, R. L., Steady magnetospheric convection selection criteria: Implications of global SuperDARN convection measurements, *Geophys. Res. Lett.*, 35, L09102, doi:10.1029/2008GL033671, 2008.

- Mechtly, E.A., and Smith, L.G., Seasonal variation of the lower ionosphere at Wallops Island during the IQSY, *J. Atmos. Terr. Phys.*, *30*, 1555–1561, 1968.
- Mechtly, E.A., and Smith, L.G., Changes of lower ionosphere electron densities with solar zenith angle, *Radio Sci.*, *5*, 1407–1412, 1970.
- Mechtly, E.A., Bowhill, S.A., and Smith, L.G., Changes of lower ionosphere electron concentrations with solar activity, *J. Atmos. Terr. Phys.*, *34*, 1899–1907, 1972.
- Mertens, C.J., Xu, X., Bilitza, D., Mlynczak, M.G., and Russell, J.M., Empirical STORM-E model: II. Geomagnetic corrections to nighttime ionospheric E-region electron densities, *Adv. Space Res.*, *51*, 575–598, doi:10.1016/j.asr.2012.09.014, 2013.
- Miller, K.L., and Smith, L.G., Horizontal structure of midlatitude sporadic-E layers observed by incoherent scatter radar, *Radio Sci.*, *10*, 271–276, 1975.
- Miller, K.L., and Smith, L.G., Incoherent scatter radar observations of irregular structure in mid-latitude sporadic E layers, *J. Geophys. Res.*, *83*, 3761–3775, 1978.
- Nygrén, T., Studies of sporadic E-layer using the EISCAT incoherent scatter radar, *Adv. Space Res.*, *9*, 573–581, 1989.
- O'Brien, T. P., Thompson, S. M., and McPherron, R. L., Steady magnetospheric convection: Statistical signatures in the solar wind and AE, *Geophys. Res. Lett.*, *29*, 1130, doi:10.1029/2001GL014641, 2002.
- Parker, E.N., Dynamics of the interplanetary gas and magnetic fields, *Astrophys. J.*, *128*, 664–676, 1958.
- Parkinson, B.W., and Spilker, J.J., *Global Positioning System: Theory and Applications Vol I*, American Institute of Aeronautics, Washington D.C., 1996.
- Piggott, W.R., and Rawer, K., *URSI Handbook of Ionogram Interpretation and Reduction, Rep. UAG-23A*, 2nd ed., World Data Cent. A, U.S. Dept. of Commer., Washington D.C., 1978.
- Primdahl, F., The fluxgate magnetometer, *J. Phys. E: Sci. Instrum.*, *12*, 241–253, doi:10.1088/0022-3735/12/4/001, 1979.
- Ruohoniemi, J.M., and Greenwald, R.A., Statistical pattern of high-latitude convection obtained from Goose Bay HF radar observations, *J. Geophys. Res.*, *101*, 21,743–763, doi:10.1029/96JA01584, 1996.
- Russell, C.T., and McPherron, R.L., Semiannual variation of geomagnetic activity, *J. Geophys. Res.*, *78*, 1, 92–108, 1973.
- Salah, J.E., and Holt, J.M., Midlatitude thermospheric winds from incoherent scatter radar and theory, *Radio Sci.*, *9*, 301–313, 1974.
- Schlegel, K., Coherent backscatter from ionospheric E-region plasma irregularities, *J. Atmos. Terr. Phys.*, *58*, 933–941, doi: 10.1016/0021-9169(95)00124-7, 1995.

- Strickland, D.J., Jasperse, J.R., and Whalen, J.A., Dependence of auroral FUV emissions on the incident electron spectrum and neutral atmosphere, *J. Geophys. Res.*, *88*, 8051–8062, 1983.
- Torr, M.R., and Torr, D.G., The seasonal behavior of the F2-layer of the ionosphere, *J. Atmos. Terr. Phys.*, *35*, 2237 – 2251, 1973.
- Turunen, T., Nygrén, T., and Huuskonen, A., Nocturnal high-latitude E-region in winter during extremely quiet conditions, *J. Atmos. Terr. Phys.*, *55*, 783–795, 1993.
- Turunen, T., Silén, J., Nygrén, T., and Jalonen, L., Observation of a thin Es-layer by the EISCAT radar, *Planet. Space Sci.*, *33*, 1407–1416, 1985.
- Wand, R.H., Seasonal variations of lower thermospheric winds from the Millstone Hill incoherent scatter radar, *J. Geophys. Res.*, *88*, 9227–9241, 1983.
- Werner, S., and Prölss, G. W., The position of the ionospheric trough as a function of local time and magnetic activity, *Adv. Space Res.*, *20*, 1717–1722, doi:10.1016/S0273-1177(97)00578-4, 1997.
- Whitehead, J.D., Production and prediction of sporadic E, *Rev. Geophys. Space Phys.*, *8*, 65–144, 1970.
- Whitehead, J.D., Sporadic E layers; history and recent observations, *Adv. Space Res.*, *10*, 85–91, 1990.
- Willmore, A.P., Exploration of the ionosphere from satellites, *J. Atmos. Terr. Phys.*, *36*, 2255–2286, 1974.